Materials & Design 216 (2022) 110553

Contents lists available at ScienceDirect

Materials & Design

journal homepage: www.elsevier.com/locate/matdes

Mix design and performance of lightweight ultra high-performance concrete

Jian-Xin Lu [a,b], Peiliang Shen [a], Hafiz Asad Ali [a], Chi Sun Poon [a,b,*]

[a] Department of Civil and Environmental Engineering, The Hong Kong Polytechnic University, Hung Hom, Kowloon, Hong Kong, China
[b] Research Centre for Resources Engineering Towards Carbon Neutrality (RCRE), The Hong Kong Polytechnic University, Hung Hom, Kowloon, Hong Kong, China

HIGHLIGHTS

- Central Composite Design method was effective in designing novel lightweight ultra high-performance concrete (L-UHPC).
- The L-UHPC prepared with micro-sized glass microsphere and lightweight aggregates had ultra high strength (>120 MPa) and low density (<1950 kg/m^3).
- The developed L-UHPC had excellent structural efficiency, superior functional and durability properties.
- The high strength lightweight microspheres and high rigidity of paste matrix contributed to great performances of L-UHPC.

GRAPHICAL ABSTRACT

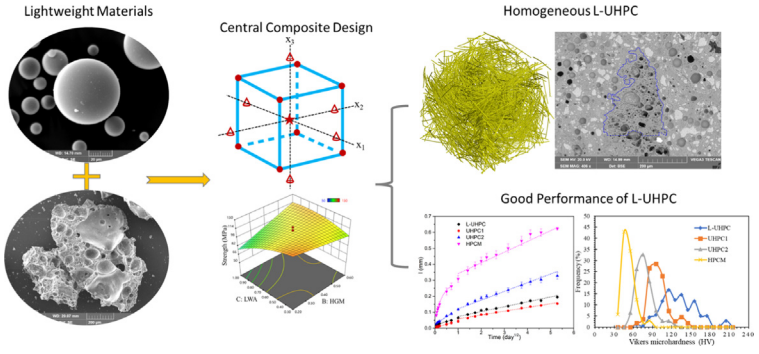

ARTICLE INFO

Article history:
Received 23 October 2021
Revised 20 February 2022
Accepted 13 March 2022
Available online 17 March 2022

Keywords:
Mix design
Lightweight UHPC
Lightweight materials
Durability
Structural efficiency

ABSTRACT

The inferior mechanical properties and durability of conventional lightweight concrete restrict its wider application. This study intended to design a novel lightweight ultra high-performance concrete (L-UHPC) using a mathematical approach, with a view to achieving low density and excellent performance. Two lightweight materials (i.e. micro-sized glass microsphere and expanded shale aggregates) were introduced in the mix design of L-UHPC. The statistical optimization via Central Composite Design was proved to be an effective method to produce the L-UHPC. The designed L-UHPC showed comparable or even superior functional and durability properties than normal-weight UHPC and high-performance cement mortar. The use of specified lightweight materials played prominent roles in ensuring the mechanical properties of L-UHPC. The high microhardness of paste matrix and the internal curing of lightweight aggregates contributed to the great durability of L-UHPC. The development of L-UHPC can provide a new solution for constructing high-performance lightweight structures and composites.

1. Introduction

There are two contrary design concepts for concrete development, one is to increase the density of the matrix as high as possible aiming to attain better performance, and the other is to reduce the density of the matrix as low as possible targeting to achieve better thermal insulation. The former is the common way to pro-

* Corresponding author at: Department of Civil and Environmental Engineering, The Hong Kong Polytechnic University, Hung Hom, Kowloon, Hong Kong, China.
E-mail addresses: jxinlu@polyu.edu.hk (J.-X. Lu), cecspoon@polyu.edu.hk (C.S. Poon).

https://doi.org/10.1016/j.matdes.2022.110553
0264-1275/

duce high strength and high-performance concrete for structural applications. The latter technique is commonly used to produce non-load bearing components, such as insulation materials. One typical concrete of using the former design concept is the ultra high-performance concrete (UHPC). A number of investigations [1–5] have tried to improve the properties of UHPC by means of increasing its packing density. The higher packing density generally gives rise to good compaction of the constitutes and results in a low porosity matrix [2,5]. Hence, the concrete can theoretically attain higher mechanical properties and greater durability. For optimizing packing density of UHPC, different models and approaches have been proposed [2,4]. Therein, the Andreasen & Andersen packing model or its modified version is the most popular model to obtain a densely solid particle packing. To upgrade this model by further considering the liquid phases, a method of high wet packing density was recently developed to optimize the design of UHPC [6]. Unlike the design of high-density concrete, ultra lightweight concrete (ULC) is also attracting a lot of interests for energy-saving purposes [7–10]. To reduce the weight of concrete, the elimination of heavy raw materials in the concrete, such as natural aggregates, is the first consideration, followed by additions of alternative porous materials with very low density [11]. Another approach to make the ULC is by incorporating a large volume of air voids in the mixture. Chemically generated gases and physically stable foam are two common types of air voids introduced into the concrete [12]. Due to the presence of porous materials and voids in the matrix, the overall density of ULC can be reduced to 1000 kg/m^3 or even lower.

In light of the opposite design concept with density towards two directions, UHPC and ULC have individually been successfully developed and put into practical applications [13,14]. However, barriers still exist to extend their application areas. One of the major deficiencies of UHPC is the high autogenous shrinkage since it usually consists of a high volume of fine powder and a very low water content [15]. Several solutions have been proposed to mitigate this issue and reduce the risk of early-age cracking, including the uses of shrinkage reducing admixture [16,17], internal curing agents [18,19], expansive agents [20,21], fibers [17,22], etc. Among these, the inclusion of internal curing materials was regarded as the most effective solution to lower the autogenous shrinkage of UHPC [15]. For the ULC or conventional lightweight concrete (LWC), the high porosity of matrix would inevitably result in poor mechanical properties and durability performance. However, with the increasing expectation for LWC in servicing as structural materials, the improvements of its strength and durability are of great importance.

The strategies for producing a high-strength and high-performance LWC mainly rely on the use of high-quality cement mortar and high-strength lightweight aggregates (LWA). Replacements of some parts of cement by pozzolanic materials (i.e. silica fume, metakaolin, fly ash and ground granulated blast-furnace) are used to make the mortar matrix more dense [23–27]. As the LWAs are the weakest components in the LWC, increasing the crushing resistance of LWAs seems to be able to enhance the mechanical properties of LWC [28]. Thus, high-strength artificial and natural LWAs, e.g. sintered fly ash [24,29], expanded clay and slate [30,31] and oil palm shell [32,33], are adopted to prepare high-strength LWC.

Aforementioned, the high-density concrete and the low-density concrete have respective advantages and disadvantages. Whether there is a compromised solution that can exploit the advantages of the high strength of UHPC and the light weight of LWC, and meanwhile, evade the high shrinkage of UHPC and low strength of LWC. Therefore, this study intended to design a novel lightweight ultra high-performance concrete (L-UHPC), aiming to achieve ultra high strength, low density and low shrinkage simultaneously. Previously, most of the structural LWC exhibited compressive strength of 40–70 MPa and structural efficiency (i.e. ratio of strength to density) of 20–40 kN m/kg [34–36]. It is of great interest to explore an effective approach for producing a structural LWC with ultra high strength and higher structural efficiency, with a view to satisfying the increasing demands of long-span structures and construction in hostile environment. In previous literature, very few studies have successfully prepared a structural LWC with strength higher than 120 MPa and density <2000 kg/m^3. Although our recent study [37] investigated the ultra high-performance lightweight paste, the lack of aggregates and the presence of high amount of binder in the mixture would be likely to induce high shrinkage. Hence, in this study, a micro-sized lightweight pozzolanic material (i.e. hollow glass microsphere) and an expanded shale-based fine LWA were innovatively combined for reducing the weight and ensuring the good performance of L-UHPC (including low shrinkage). Moreover, mathematical and statistical approach was adopted to optimize the contents of these two lightweight materials in the production of L-UHPC. Previously, many investigations have primarily focused on developing mix design methods for conventional cement concrete [38–40], UHPC [2,41,42] and LWC [43–45]. However, there are no feasible mix design methods for producing L-UHPC.

This study, at the first time, attempted to develop L-UHPC with lightweight materials using Central Composite Design (CCD) methodology, which is one of the most important design methods used in optimization experiments [46]. The CCD method is also one of the powerful mathematical and statistical method of prediction in mixture optimization of concrete. The advantage of this experimental design approach is able to evaluate the influence of the independent variables on the responses with a minimal number of concrete experiments [47,48], which is important for reducing labor and material consumptions. Moreover, the optimization of concrete mixtures can utilize the materials' full potential to achieve satisfactory performance or a longer service life. Therefore, the CCD method has been successfully used to design mortar or concrete for multi-objective optimization [49–51]. For example, Bankir and Sevim [49] used the CCD method to optimize the dependent variables and maximize the mechanical properties of fiber-reinforced concrete. Hassan et al. [50] obtained an optimum high strength concrete blended with a supplementary cementitious material. Nunes et al. [51] made a mixture design of self-compacting mortar using CCD method to maximize durability and minimize cost. Recently, several investigations have applied the CCD method in the design of UHPC [18,52–54], however, it remains unknown whether the CCD method is feasible to design an L-UHPC. Hence, it would be of interest to prepare L-UHPC using CCD technique and explore the optimum combination of lightweight binder and aggregates to obtain desirable properties of L-UHPC. In this study, the physical, functional and durability properties of the produced L-UHPC were also evaluated and compared to a normal-weight UHPC with equal strength and a high-strength cement mortar. The effectiveness of the design method and the roles of lightweight media were discussed by means of X-ray CT, element distribution mapping and micro-indentation techniques.

2. Materials and methods

2.1. Materials

A type of CEM I 52.5 Portland cement (Hong Kong Green Island Cement) was adopted as the main binding material. Silica fume (SF) sourced from Mainland China was used to prepare a high-quality paste. Also, the HGM (hollow glass microsphere) and LWA (expanded shale grains) were obtained from manufacturers

from Mainland China and they were incorporated in the mixture for reducing the weight of the concrete. The HGM was employed as a pozzolanic material and the LWA acted as fine aggregates in the mixture. The size of LWA was ranged from 0.3–1.18 mm. The selection of the specified shale LWA was due to its higher strength and reactivity compared to other LWAs, such as expanded clay LWA [55]. The 24-hour water absorption of LWA was 5.8%. This value was low due to the smaller particles of LWA and the presence of small pores in the LWA matrices (Fig. 3). The dry loose bulk density of LWA and the apparent density of pre-soaked LWA were 650.7 and 1587 kg/m^3, respectively. River sand (RS, 0.3–1.18 mm) after washing by tap water was also used as a comparison (loose bulk density: 1675 kg/m^3). Both of LWA and RS constituted 55 wt% of 0.3–0.6 mm size aggregate and 45 wt% of 0.6–1.18 mm size aggregate. Copper coated straight steel fibers, which had a density of 7.8 kg/m^3, diameter of 0.22 mm and length of 13 mm, were incorporated into the concrete mixes to ensure a high flexural strength. A polycarboxylic ether superplasticizer (SP) from BASF was used for preparing a low water-to-binder (w/b) ratio binder mixture.

The chemical compositions of the materials used were determined by an X-ray fluorescence spectrometer (Rigaku Supermini200) and the results are listed in Table 1. It should be noted that the HGM was a soda-lime-silica glass material, rich in SiO_2, CaO and Na_2O. A laser diffraction particle size analyzer (Malvern Mastersizer 3000E) was employed to determine the particle size distributions of the cement and HGM. Due to the extremely fine particles of the SF, its particle size was measured by a Zetasizer (Malvern, Nano-ZS90). The results are presented in Fig. 1, showing that the SF and HGM had narrow particle size distributions and the cement particles filled the size gap between the SF and the HGM.

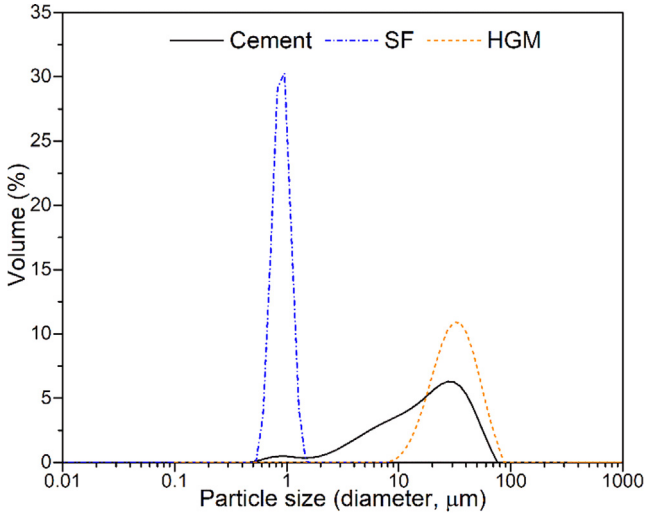

Fig. 1. Particle size distributions of cement, SF and HGM.

2.2. Characteristics of HGM and LWA

The crystallinity of HGM and LWA were measured by X-ray diffraction (XRD) analysis (Fig. 2a).

As shown, the shale LWA contained some crystalline phases, including quartz and hercynite ($FeAl_2O_4$, PDF#34-0192). Each content of these crystalline phases in the LWA could be analyzed by quantitative XRD. 20 wt% of the powdered LWA were replaced by corundum as an internal standard. Topas 4.2 software was performed to analyze the XRD data by Rietveld refinement method. Hence, the LWA was consisted of quartz (17%), hercynite (3.4%) and amorphous phase (79.6%). Based on the chemical composition of LWA, the major minerals in the amorphous phase were rich in SiO_2 and Al_2O_3. By contrast, the HGM did not exhibit any crystalline peaks in the diffraction pattern, which indicates a completely vitreous structure. Fig. 2b shows the pozzolanic reactivities of HGM and LWA determined by the Chapelle test [56]. The results indicate that 1 g of HGM was able to consume more than 1 g of $Ca(OH)_2$ (1.453 g). The high $Ca(OH)_2$ consumption is an indication of high pozzolanic reactivity in the alkaline cementitious system. Hence, it is envisaged that the HGM with vitreous structure would exert a high pozzolanic reaction in the cementitious matrix. This result is consistent with a recent study [57]. Compared with the HGM, per gram of LWA could react with a much smaller amount of $Ca(OH)_2$ (605 mg). Even so, this value of $Ca(OH)_2$ consumption was higher than some supplementary cementitious materials, such as fly ash and glass powder [56]. This also implies that the surface of LWA would involve in pozzolanic reaction with the alkaline hydrates.

The morphologies of HGM and LWA were observed by scanning electron microscopy (SEM, Tescan VEGA3). The SEM images shown in Fig. 3 demonstrate that the HGM consisted of spherical particles with a smooth surface. Most of the intact particles were within the size range of 10–100 μm. As the HGM had a very low density (420 kg/m^3), its structure should be hollow. The smooth texture,

Table 1
Chemical compositions and physical properties of materials (wt%).

Compositions	Cement	SF	HGM	LWA	RS
SiO_2	19.0	79.4	80.5	62.4	94.4
Al_2O_3	5.68	0.91	0.86	20.4	2.18
CaO	65.8	11.1	8.36	0.68	1.06
MgO	0.97	4.27	0.14	2.75	0.32
K_2O	0.66	2.94	0.08	4.5	0.97
P_2O_5	0.16	0.13	0.09	0.21	0.09
Fe_2O_3	3.12	0.43	0.06	6.79	0.54
Na_2O	/	/	9.71	1.03	/
SO_3	4.03	0.58	0.19	0.08	0.04
Physical properties					
Specific gravity	3.15	2.08	0.42	2.35*	2.41*
Average particle size (μm)	22.7	0.97	36.3	/	/

Note: * means the powdered form of sample (true density).

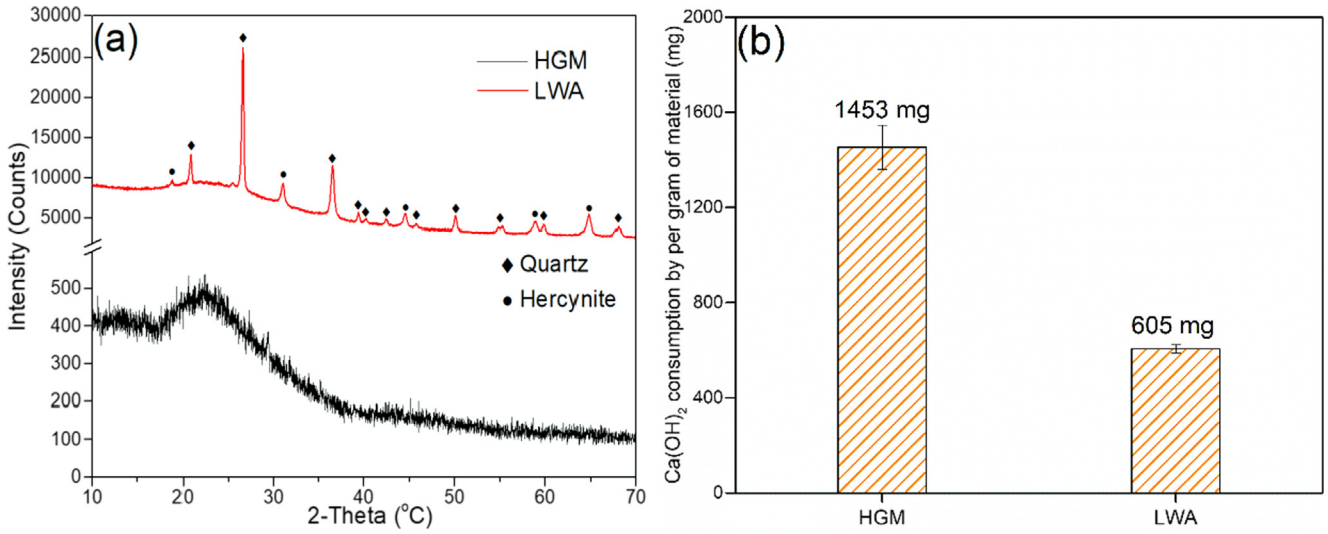

Fig. 2. (a) XRD patterns and (b) Pozzolanic reactivity of HGM and LWA.

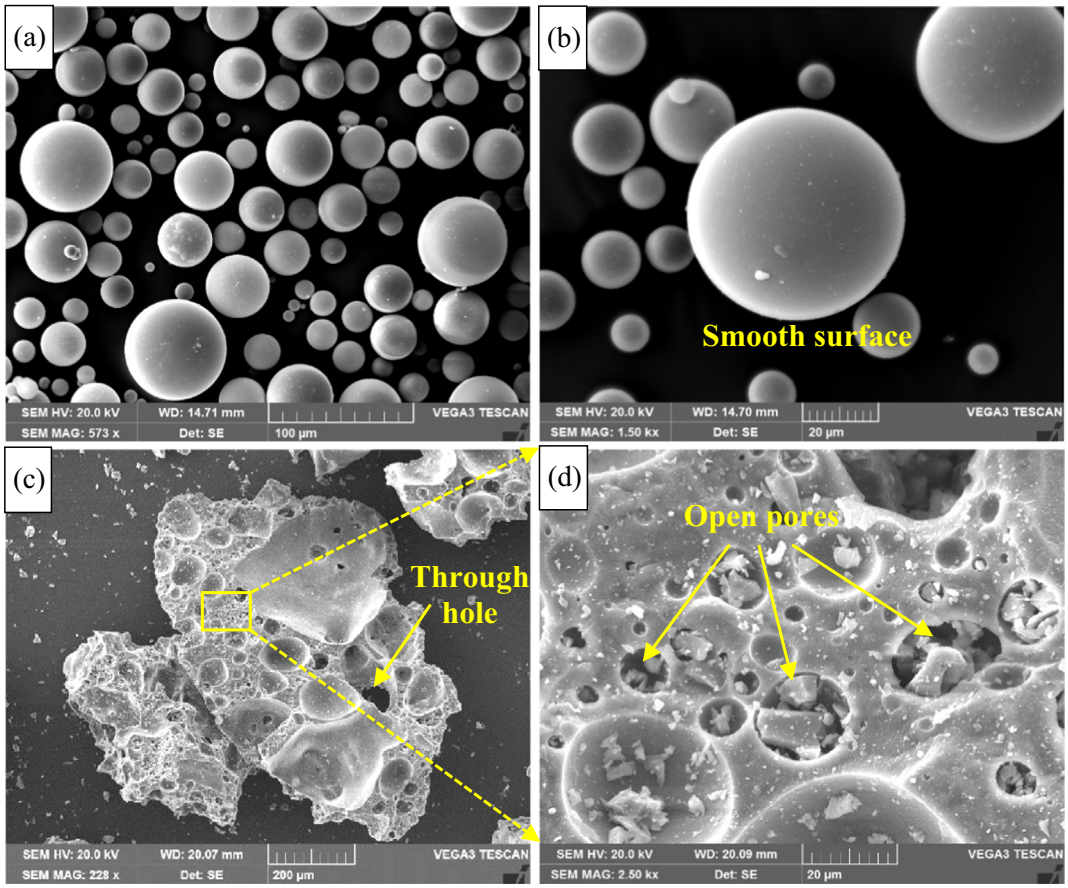

Fig. 3. Morphologies of HGM (a and b) and LWA (c and d).

vitrified structure and spherical shape of HGM would enable non-absorbent and lubricating effects for cement-based matrices. As the vitrified HGM was micro-sized (average size: 36.3 μm) and unbroken, it had high gas isostatic compression strength (20.7 MPa). Fig. 3c and 3d also present the appearance of LWA. Many cavities were observed on the surface of LWA because of the crushing process during production. Furthermore, some through voids were found in individual particles of LWA. A closer examination shows open pores with different sizes embedded in the matrix of LWA. These pores would be able to absorb water. Also, the rough surface of LWA would increase the contact area with the cement paste.

2.3. Mix design

2.3.1. Design concept

This study aimed to develop an L-UHPC with a view to achieving high strength (>120 MPa) and light weight (<2000 kg/m^3). Firstly, a very strong mortar system should be designed for the preparation of L-UHPC to attain high strength. It is known that the UHPC composite possesses excellent mechanical properties and durability due to its dense structure. Thus, the UHPC matrix was used in this study as the main body of L-UHPC. However, for the UHPC system, a large amount of cement remains unhydrated because of the extremely low water content in the mixture [58]. This provides an opportunity to replace a part of the high-density cement by a lightweight pozzolanic material. Furthermore, fine sand is commonly used as a filler in the UHPC. The presence of sand with a high density contributes to the high weight of UHPC matrix. Therefore, a lightweight fine aggregate was further introduced as a replacement of sand. The water absorption of the LWA used in this study was lower than conventional LWAs. This is because the particle size of LWA was small and the LWA was embedded with small pores, while the large pores were eliminated by the crushing process (as shown in Fig. 3). Although the water absorption of the LWA was low, the benefit of internal curing effect would still be expected. A recent study [59] reported that the incorporation of porous aggregates with a 24-h water absorption of 5.4% was able to provide very good internal curing and reduce autogenous shrinkage of UHPC significantly. Finally, within the reference UHPC system (Table 2), a lightweight pozzolanic material (i.e. HGM) and a lightweight fine aggregate (expanded shale grains) were jointly used to reduce the weight of the paste and aggregates, respectively, for the production of L-UHPC.

2.3.2. Mathematical modeling

To optimize the design of the concrete mixture, a mathematical and statistical technique was adopted, namely Central Composite Design (CCD). The aim of the CCD method was to establish functional interactions between the variables and responses via design of experiments, and then optimize the variables by statistical analysis for predicting desirable responses [46]. This method is generally adopted when there are several input parameters (variables) affecting the output (responses). The benefit of selecting CCD method in this study was able to evaluate the influence of the independent variables on the responses with minimum trial mixtures. As mentioned, OPC, HGM and LWA would be the most influential materials in determining the weight of concrete. Thus, the amounts of the main cementitious material (i.e. OPC) and two lightweight materials (i.e. HGM and LWA) were adjusted and optimized for the preparation of L-UHPC. These three-level factors (amounts of OPC, HGM and LWA) were set as variables. The constraint conditions of variables are listed in Table 3. Commonly, the maximum replacement ratio of cement by pozzolanic materials is not higher than 60% by volume [60,61], thus the OPC variable was set from 0.4 to 1.0, the corresponding maximum value of HGM variable was taken as 0.6. Since the RS can be 100% replaced by the LWA, the upper limit of LWA variable could reach 1.0. The lower conditions of variables of HGM and LWA were determined to ensure the reduction in sample density. The density and compressive strength were the responses. The experimental points and response results are shown in Fig. 4 based on rotatable design, which means that the responses resulted from factorial and axial points would have the same variance. The variables were standardized and coded, the values were in the range of −1.0 to 1.0. For example, 0.2 of B means 20% of OPC are replaced by HGM in volume, 1.0 of C stands for the full replacement of RS by the same volume of LWA based on the proportion of Table 2. The CCD method can efficiently reduce the number of trial mixtures when quantitative factors (3 in this study) are introduced in experiment design [47]. Therefore, based on the CCD model for three experimental factors (Fig. 4), the total number of experiments was determined according to the equation: $N = 2^k + 2k + m$, where k is the number of the independent variables, 2^k represents the factorial points, 2 k stands for the axial points and m is the number of the experiments in the central points (k = 3 and m = 3 in this study). Therefore, 17 experiments were realized to create the optimum values of and achieve the desirable properties of responses. The proportions of 17 mixtures (8 factorial points, 6 axial points and 3 replicates of central points) were designed based on the CCD by using the Design Expert 8.0 software (Table 4). Except the above three variables, other parameters in the mix proportions (e.g. *w*/*b*, SF content) were kept at the same values as those in the reference UHPC (Table 2). After curing under the conditions described in Section 2.2.3, the varying density and compressive strength were attained as responses. Based on the experimental points and the responses, the data can be fitted by a quadratic model as follows:

$$Y = \beta_0 + \sum \beta_i x_i + \sum \beta_{ii} x_i^2 + \sum \beta_{ij} x_i x_j \quad (1)$$

where β_0, β_i, β_{ii} and β_{ij} are the coefficients intercept of the equation; x is variable; y is predicted response. The applicability and reliability of the developed response surface quadratic model was evaluated by analysis of variance (ANOVA), including some model parameters, such as model p-value (probability value) and coeffi-

Table 2
Proportion of reference UHPC (kg/m^3).

Mix	OPC	SF	Water	SP	Fiber	RS	*w*/*b*	Compressive strength (MPa)
UHPC1	907	246	180	34	117	1153	0.18	186.4

Note: The water content of SP was 80%. The dosage of steel fiber accounted for 1.5% volume of mixture. The compressive strength of UHPC was obtained after steam curing (90 °C) for 2 days.

Table 3
Variables and responses in CCD.

Variables		Constraint condition			Responses (y)
Coded	Materials	Minimum (−1)	Mean (0)	Maximum (+1)	
A	OPC	0.4	0.7	1.0	Density, Strength
B	HGM	0.2	0.4	0.6	
C	LWA	0.3	0.65	1.0	

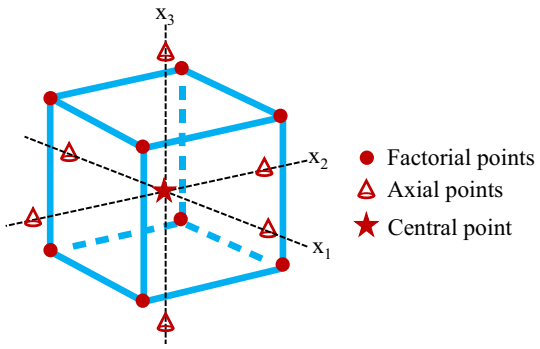

Fig. 4. Distribution of factorial, axial and central points in CCD (rotatable design).

cient of determination. Furthermore, the influence of each variable (in-put parameters) on the responses (out-put parameters) were analyzed by ANOVA. Afterward, numerical optimization of an L-UHPC mixture was performed under the criteria of adequate density and maximum strength. Lastly, the optimized proportion was verified by experiment to make sure the accuracy of the theoretical prediction.

2.3.3. Mix preparation

For preparing the samples, all the dry cementitious materials (OPC, SF, HGM) were pre-mixed in a laboratory mixer for 3 min. Then, the pre-wetted LWA (immersion in the water including mixing water and absorbed water by LWA for 24 h according to Ref. [62]) was placed into the mixer with SP together. Thereafter, the materials were blended for 3 min at a slow speed (122 rpm) and 8 min at a high speed (430 rpm). Lastly, the steel fiber was added and mixed for another 2 min at a slow speed to obtain a homogenous slurry. The fresh mixtures were cast into steel moulds and then transferred to a vibrating table for compaction for 30 s. The surfaces of moulds were covered by plastic sheets to maintain the moisture of mixtures. After hardening for 24 h in the laboratory environment (23 ± 2 °C and 50% relative humidity), the specimens were demoulded and placed into a 90 °C steam chamber for 48 h as recommended [63].

2.4. Methods

2.4.1. Surface-dry density and mechanical properties

Prism samples with a size of 40 × 40 × 160 mm^3 were cast for determining the density and mechanical properties. After steam curing for 48 h, the samples were cooled down to ambient temperature. The surface-dry density of the samples was measured by weighting their mass in air and testing their volume in water as specified in BS EN 12390-7:2019 [64]. The mechanical properties of the samples including compressive and flexural strengths (centre-point loading) were carried out according to BS EN 1015-11:2019 [65]. The loading rates for the compressive and flexural strengths were 0.5 mm/min and 0.6 MPa/s, respectively. Three samples were measured to obtain an average value.

2.4.2. Thermal conductivity and acoustic properties

The thermal conductivity of the samples was measured by a transient plane heat source (hot disc) method complying with BS EN ISO 22007-2 [66]. A thermal conductivity meter (Hot Disk M1) equipped with a Kapton sensor 8563 (radius 9.9 mm) was employed for testing. The testing range was from 0.03 to 40 W/(mK). Surface-dry specimens with a size of 40 × 40 × 40 mm^3 were used for measurement. For each mixture, 15 values were tested to calculate an average result.

The acoustic properties of samples were tested by an impedance tube (Brüel & Kjær, Denmark). Sound absorption and sound transmission loss (TL) of the samples were measured according to ASTM E1050 [67] and ASTM E2611 [68], respectively. Circular specimens with a dimension of 98 mm diameter and 20 mm thickness were prepared for testing. Before measurement, the specimens were dried in an oven chamber at 40 °C for 3 days to remove surface moisture. Blu-tack was used to seal the gaps between the specimens and the tube wall to avoid noise leakage. Sound absorption coefficient and TL were acquired and processed at frequency range of 200–1600 Hz in a computer. Three specimens were tested for obtaining an average result.

2.4.3. Ion permeability and water sorptivity

The resistance to chloride-ion penetration was determined to understand the ion permeability of samples in accordance with ASTM C1202 [69]. After curing, the cylinder samples without fibers were cut into slices of Φ100 mm × 50 mm for testing. Then, the slice specimens were sandwiched in cells with 3% NaCl solution and 0.3 M NaOH solution in two sides. A voltage of 60 V was exerted on the cells to accelerate the electrical conductance. The values of cumulative charge passed over 6 h were recorded. Qualitative indications of the chloride ion penetrability were described in the above ASTM standard. Although the electrically accelerated test has limitations, it is still one of the most effective ion permeability tests, even for UHPC [5]. In order to confirm the accuracy of

Table 4
Experimental points and responses.

Mix	OPC	HGM	LWA	Density (kg/m^3)	Strength (MPa)
1	0.70	0.06	0.65	1972	94.8
2	1.00	0.20	1.00	1931	86.1
3	0.70	0.40	1.24	1828	82.8
4	0.40	0.20	1.00	1805	47.6
5	0.70	0.40	0.06	1907	96.6
6	0.70	0.40	0.65	1963	111.0
7	0.70	0.74	0.65	1893	115.5
8	1.00	0.60	0.30	1902	97.9
9	0.20	0.40	0.65	1744	64.1
10	1.00	0.20	0.30	2135	127.8
11	0.40	0.60	1.00	1764	92.2
12	0.70	0.40	0.65	1923	111.5
13	0.40	0.60	0.30	1712	93.5
14	1.20	0.40	0.65	1981	108.1
15	0.70	0.40	0.65	1964	116.8
16	0.40	0.20	0.30	1973	108.0
17	1.00	0.60	1.00	1937	115.2

Note: Table 4 only shows the coded variables as other parameters in the mix proportions were kept at the same values with those in the reference UHPC (Table 2).

Table 5
ANOVA results of model parameters.

Responses	Model F-Value	Lack of Fit	Model p-value	R^2	Adjusted R^2	Predicted R^2	Adequate Precision
Density	28.66	1.89	<0.0001	0.95	0.91	0.84	18.4
Strength	16.87	6.85	0.0001	0.91	0.86	0.70	14.0
Implication	Significant model	Insignificant	Significant model terms	Good fitting	Reasonable agreement		Adequate signal

the permeability tested by rapid electricity conductive, the rate of absorption (sorptivity) of water was further tested to understand the susceptibility of samples to water penetration. The test method was conducted according to ASTM C1585 [70]. The specimens used for this measurement were the same with the acoustic properties test. Only one surface of the specimen was exposed to water. The increased mass of specimens resulting from water absorption was recorded as a function of time. Due to the low water absorption of specimens, the measurement was performed up to 110 days at room temperature (23 ± 2 °C).

2.4.4. Autogenous and drying shrinkages

The autogenous shrinkage of the samples was monitored by flexible corrugated tubes according to ASTM C1698 [71]. The fresh mixtures were filled and sealed in the polyethylene tubes to prevent moisture loss. To remove entrapped air, the corrugated moulds were vertically cast under vibration conditions. The measurement of autogenous strain was recorded after setting up to 72 h at room temperature (23 ± 2 °C). The changes in length were recorded at every minute interval by a data logger.

The drying shrinkage of hardened samples after curing was measured in conformance with the requirements of ASTM C596 [72]. The fresh mixtures were cast into prism moulds with a dimension of 25 × 25 × 285 mm^3. After 24 h, the specimens were removed from the moulds and transferred into a steam chamber for 48 h at 90 °C (same curing conditions with other tests). It should be noted that the testing of drying shrinkage after curing aimed to evaluate the long-term shrinkage of almost completely hydrated samples under drying condition except the early-age autogenous shrinkage. The initial length measurement was taken after cooling down of the specimen to ambient temperature. Then, the specimens were placed in a drying chamber at 25 °C and 50% humidity. The length changes of the specimens after specified time of drying (4, 11, 18, 25, 32 and 46 days of storage) were recorded according to the above ASTM standard. The mean drying shrinkage values of the specimens were calculated based on the results of three specimens.

2.4.5. Microstructure tests

The pore structure of samples was evaluated by mercury intrusion porosimetry (MIP). The device (Micromeritics AutoPore IV 9500 Series) was working at a maximum mercury intruding pressure of 207 MPa into the pores. The smallest pore size of 7 nm could be detected. To prepare specimens for MIP test, the samples after curing were cut into thin slices and soaked into ethanol for one week. Then, the slices were transferred to a vacuum oven at 60 °C to remove the residual ethanol. Afterward, the slice samples were crushed into small pieces of around 5 mm for testing. For this test, it is reminded that ink-bottle effect may affect the porosity since the detected pores were smaller than they actually were [73].

The morphology of fractured sample was observed by SEM (Tescan VEGA3). Small fragments of sample were collected after the strength tests. Before coating with gold, the hydration of the sample was terminated as described above. For backscattered electron (BSE), thin slice samples were embedded in an epoxy resin, followed by polishing with different grits of papers (320, 600, 1200 grits). Then, finer diamond papers (grits 9 μm, 3 μm, 0.05 μm) were used for further polishing step by step to attain more smoother surface. After completed, the polished samples were dried in a 60 °C vacuum oven until testing. Prior to SEM/BSE observation, the samples were coated by carbon. The SEM/BSE measurements were carried out at 20 kV voltage and a working distance of 10–16 mm. Meanwhile, elemental distributions on the sample surface were determined by an energy dispersive X-ray spectroscopy (EDX) detector.

The micro-mechanical property of cement paste in the samples were tested by using a digital Vickers microhardness tester (HVX-1000A). The sample preparation of microhardness test was the same with the SEM/BSE. A 25-g force was loaded on the paste matrix by a diamond indenter for 14 s. Then, the Vickers microhardness (HV) could be calculated based on diagonal length of indentation and the angle of diamond indenter. As the cementitious material is an inhomogeneous matrix, the microhardness of different zones would vary significantly, more than 100 indentation points were tested for each mixture to acquire a statistical distribution analysis.

To understand the homogeneity of constituents in the L-UHPC, a high-resolution X-ray computed tomography (CT, YXLON FF35) was adopted to reveal the distributions of steel fibers and LWA in the matrix. Cubic sample with a dimension of 40 × 40 × 40 mm^3 was used for the measurement. The X-ray tube was run at a voltage of 200 kV and a current of 65 μA. During a 360° rotation of scanning, 1800 projections of two-dimensional (2D) images were integrated. Then, the three-dimensional (3D) volumetric structures were created via real-time reconstruction software (CERA). Finally, VGStudio MAX was used to observe and analyze the 2D and 3D images.

3. Experimental results

3.1. Mix design by CCD

3.1.1. Accuracy of model

As mentioned, the experimental results of density and compressive strength in Table 4 were analyzed by the response surface quadratic model. To verify the applicability and reliability of the developed model, analysis of variance (ANOVA) was performed. The ANOVA was also intended to understand the significance of the variables and the reliability of the fitted results. The variance was calculated by the variation between the experimental (actual) and predicted responses. Some parameters of ANOVA could be obtained as shown in Table 5.

A model p-value of <0.05 (low probability) indicates that the model terms are significant, and vice versa. Hence, the significant model terms were retained and the insignificant model terms were excluded. After simplifying the model, empirical relationships between the responses (density and strength) and the variables were expressed by Eqs. (2) and (3). It can be noted that the coefficient of determination (R^2) of density and strength was higher than 0.9, which denotes the good fitting between the model and the actual data. The good relations between the predicted value and

the actual value are presented in Fig. 5. The Model F-values of density and strength in this case imply that the models were significant. There was only a 0.01% chance (Model p-value) that a Model F-Value of this level could occur because of noise. The low Lack of Fit F-values of 1.89 and 6.85 suggest that the selected models had insignificant lack-of-fit (insignificant relative to the pure error). Thus, the non-significant lack of fit reveals that the models were good to fit. In addition, the Predicted R^2 was in reasonable agreement with the Adjusted R^2 for both the density and strength, representing a satisfactory adjustment of the quadratic models to the experimental data. The Adequate Precision was the signal to noise ratio. The ratios in this study were greater than 4 (adequate signal), which indicate that these models could be used to navigate the design space. Overall, the ANOVA results show a reliable confidence in the prediction of density and strength.

$$\text{Density} = 1944.63 + 76.79A - 48.30B - 30.67C + 57.38BC - 27.43A2 - 25.67C2. \quad (2)$$

$$\text{Strength} = 110.29 + 11.69A + 4.69B - 8.00C + 14.76BC - 8.16A^2 - 6.88C^2. \quad (3)$$

Note: A is amount of OPC, B is amount of HGM, C is amount of LWA.

3.1.2. Influences of variables on responses

The perturbations of the density and the strength due to the variables are shown in Fig. 6. As seen in Fig. 6a, the curvatures of curves A and B were much steeper than that of curve C in the density results, indicating that the density was more sensitive to the OPC and HGM contents. The density decreased considerably with the decreasing OPC content or the increasing HGM content. The effectiveness of using LWA was less significant in the reduction of density than the use of HGM because the pre-soaked LWA had a much higher density than the HGM (1587 kg/m^3 vs. 420 kg/m^3). However, it turned to opposite perturbations in the case of compressive strength. The varying contents of LWA seemed to have a larger influence on the strength than the HGM content. If the LWA content was increased to beyond a certain value, the compressive strength would be reduced considerably. This trend was contrary to that of the OPC. The use of a lesser amount of OPC resulted in a lower strength due to the reduced volume of hydrates. As the LWA containing big pores had a poor strength, too much LWA would lead to low strength. It is interesting to note that the compressive strength was gradually increased with the increasing amount of HGM despite a large quantity of voids was associated with HGM. The structure of HGM might be responsible for this behavior (to be discussed later). Overall, from the 3D plot of the responses shown in Fig. 6c and d, in order to attain light weight and ultra high strength simultaneously, the amount of HGM should be controlled at a high volume (60% replacement of OPC in this study) while the LWA content should not be too high (<100% volume of RS).

3.1.3. Optimization of L-UHPC mixture and validation

The developed model has been demonstrated to possess high applicability and reliability based on the results of 17 mixtures (see Table 4). However, the predicted optimal proportion derived from the developed model needs to be validated by experimental results. After an adequate model was obtained, numerical optimization was conducted to create an optimized proportion with a view to achieving a mixture with an appropriate density and high strength. According to the numerical optimization, the design space was going to explore prompt amounts of variables to reach the pre-set goals for each response. The criteria for optimizing the mixture are shown in Table 6. The density was set to <2000 kg/m^3 and the strength was maximized in the range of 100–150 MPa. As a result, the theoretical optimization of variables was created in Table 7, and the counter plot of optimized mixture is shown in Fig. 7. The experimental mixture was conducted and the actual density and strength are listed in Table 7. The low deviations between the predicted value and the actual values further indicate that the precision of the developed model was accurate.

As mentioned, the precision of the developed model was accurate as the predicted value of theoretically optimized mixture were closely similar to the actual value. This indicates that the CCD was feasible to design concrete mixture. To further verify the optimum proportion, two randomly-selected proportions were prepared to compare with the optimized proportion. The experimental results are shown in Table 8. It is found that the two random mixtures had lower strength values than the optimum mixture, regardless of the higher or lower density value of the former, which confirms the finding of the optimized proportion. The satisfactory performance (density $<$1950 kg/m^3 and strength $>$120 MPa) was obtained for the L-UHPC, however, other properties of the optimum L-UHPC mixture are unknown. To this end, the comprehensive properties of the L-UHPC should be evaluated. The normal weight UHPC and high-performance cement mortar (HPCM) were also prepared for comparison. Thereinto, UHPC1 had a higher strength and UHPC2 was designed to have a same grade strength with the L-UHPC, whereas the HPCM was expected to have a lower strength than the L-UHPC. The proportions of UHPC2 and HPCM were the same with that of UHPC1 except the water and SP contents. The mix proportions of these mixtures are listed in Tables 2 and 9.

3.2. Physical, functional and durability properties of developed L-UHPC

3.2.1. Surface-dry density and mechanical properties

Fig. 8 shows the density and mechanical properties of developed L-UHPC, UHPC and HPCM. For the surface-dry density results, the L-UHPC had the lowest value of 1929 kg/m^3 while the UHPC1 had the heaviest weight of higher than 2400 kg/m^3. With the increase of water content in the mixture, the density values of UHPC2 and HPCM decreased. As a result, the corresponding compressive and flexural strengths were reduced significantly. The presence of voids in the HGM and LWA was responsible for the low density of L-UHPC. However, the mechanical properties of L-UHPC were comparable or even superior to the UHPC2 with a higher density. The compressive and flexural strengths of L-UHPC could reach 123 MPa and 16 MPa, respectively, which met the minimum strength requirement of UHPC [74]. Furthermore, according to JGJT 12-2019 standard [75], the upper limit of oven-dry density of lightweight aggregate concrete should not exceed 1950 kg/m^3. Therefore, the L-UHPC mix could be qualified as an ultra high-performance lightweight concrete. These results also reveal that the dual incorporation of lightweight HGM as a pozzolanic material and LWA as a fine aggregate was effective in reducing density and attaining ultra high strength.

One major benefit of using L-UHPC in structural elements is to reduce the dead load. The structural efficiency (strength/density) of the developed L-UHPC in this study was 63.6 kN·m/kg, which was much higher than other high strength lightweight concrete (20–40 kN·m/kg) reported in previous studies [29,32,36,76]. Also, at the same grade strength, the L-UHPC had higher structural efficiency than the corresponding UHPC2 (54.8 kN·m/kg). The higher structural efficiency represents a higher material efficiency of concrete, which implies a lower cost of foundation, a saving of steel reinforcement and a longer possible span of structure [77].

3.2.2. Thermal conductivity and acoustic properties

The thermal conductivities of L-UHPC, UHPC and HPCM are presented in Fig. 9. When the strength was decreased from UHPC1 to

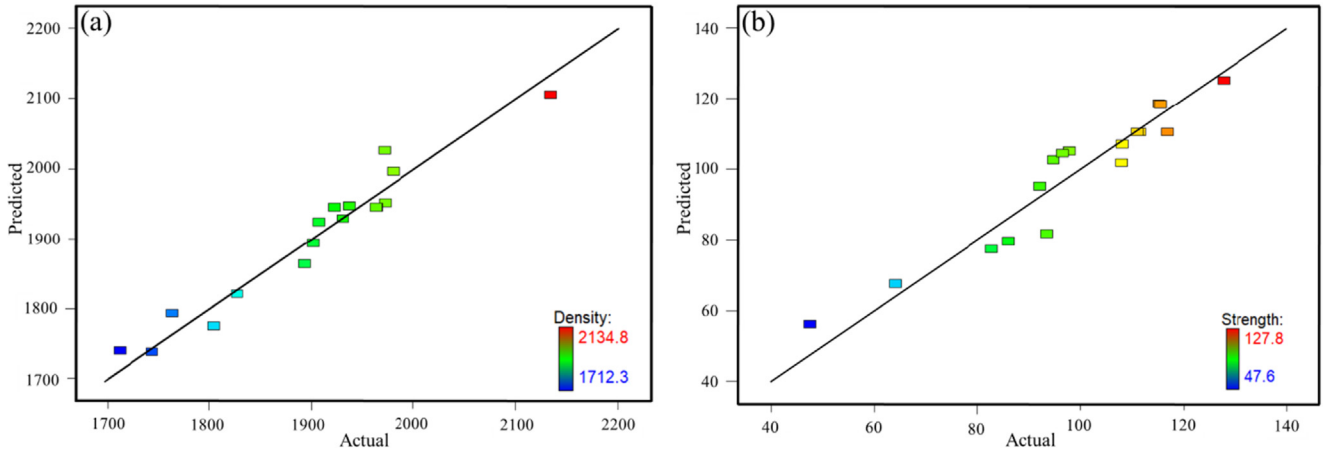

Fig. 5. Relation between predicted value and actual value, (a) Density and (b) Strength.

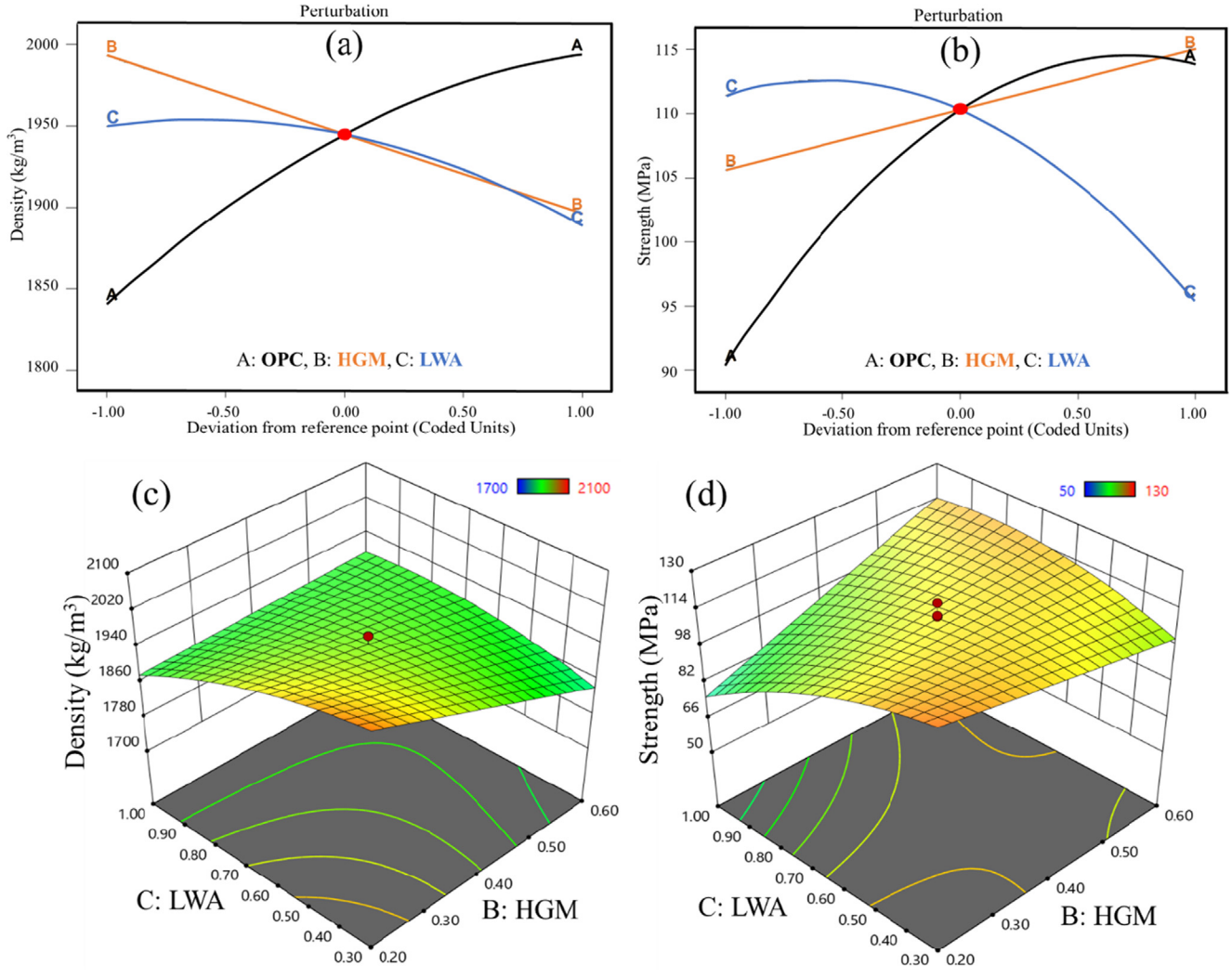

Fig. 6. Influences of variation on the density (a, c) and compressive strength (b, d) of samples (c and d are 3D plot of responses, OPC = 0.70).

HPCM, the thermal conductivity was also reduced. This reduction was related to the lower volume of quartz sand due to the increasing volume of water in the mixture. The large amount of quartz sand with a very high thermal conductivity (18.4 W/mK [78]) contributed to a higher thermal conductivity of UHPC (>2.0 W/mK). The results are consistent with the findings of previous studies [79,80]. On the contrary, the water has a much lower thermal conductivity (around 0.6 W/mK [81]), thus the HPCM prepared with higher *w*/*b* ratio exhibited a lower thermal conductivity than the UHPC. For the L-UHPC, its thermal conductivity was 1.0 W/mK, which was less than half in comparison with those of UHPC. One reason is the elimination of quartz sand in the mix. The other

Table 6
Criteria for optimization of L-UHPC mixture.

Variables and response	Lower limit	Upper limit	Goals
OPC	0.4	1.0	In range
HGM	0.2	0.6	In range
LWA	0.3	1.0	In range
Density	1700	2000	In range
Strength	100	150	Maximize

explanation is that the presence of voids in the HGM and LWA impeded the conduction of heat in the matrix. Fig. 9b shows the thermal conductivity linearly decreased with the decrease of density.

The acoustic properties of the samples, including sound absorption and transmission loss, are shown in Fig. 10. The absorption coefficient denotes the ratio of the absorbed energy to the total incident energy. Obviously, the UHPC and HPCM had similar low absorption coefficients, which can be attributed to their dense structure. In contrast, the L-UHPC exhibited the most effective absorption coefficient in the frequency range of 200–1600 Hz. Particularly at frequencies of 500–1000 Hz and 1300–1600 Hz, the L-UHPC showed high intensities of sound absorption. This behavior might be due to the small acoustical cavities were generated on the truncation surface when the two lightweight materials (i.e. HGM and LWA) were incorporated into the mixture. The micro-voids of HGM in combination with the inter-particle pores in LWA were beneficial to consuming sound energy. The improved acoustic absorption achieved was similar to the findings for other lightweight concrete prepared with porous materials (e.g. bottom ash and cenosphere) [82,83].

Fig. 10b shows the sound transmission loss values of the samples. The L-UHPC incorporated with HGM and LWA had a similar ability to insulate sound as compared to the UHPC and HPCM. The sound transmission losses of all the samples were larger than 35 dB. The UHPC and HPCM had a high density with a strong resistance to sound penetration. Although a lot of voids were present in the L-UHPC, they did not impact the sound insulation property significantly. This is because the HGM and the LWA were dispersed uniformly in the matrix, and few connective channels were formed to facilitate the sound transmission. Furthermore, the denser UHPC paste in the L-UHPC could hinder sound propagation.

3.2.3. Ion permeability and water sorptivity

The chloride ion permeability and the water sorptivity of the samples are shown in Fig. 11. Fig. 11a shows although HPCM exhibited the highest total passed charge among the four mixtures, the value was still in the range of "very low ion penetrability" (<1000 C). Much lower charge passed through the other UHPC mixtures, and according to ASTM C1202 [69] these values of charge passed indicated the negligible chloride ion penetrability. The lack of pore solution in the UHPC owing to its very low *w*/*b* ratio impeded the electric conductivity in the matrix. The highly dense matrix and the lack of water in the UHPC contributed to the high resistance to ion penetration. The very low porosities of UHPC supported these results (to be discussed in Section 3.3.1). Encouragingly, the L-UHPC had a comparable value of passed charge to the UHPC1. This means that the L-UHPC possessed a similar resis-

Table 7
Optimization of variables, theoretical and experimental responses.

OPC	HGM	LWA	Density (kg/m^3)			Strength (MPa)		
			Predicted	Actual	Deviation	Predicted	Actual	Deviation
0.92	0.6	0.82	1944	1929	0.79%	121	123	1.62%

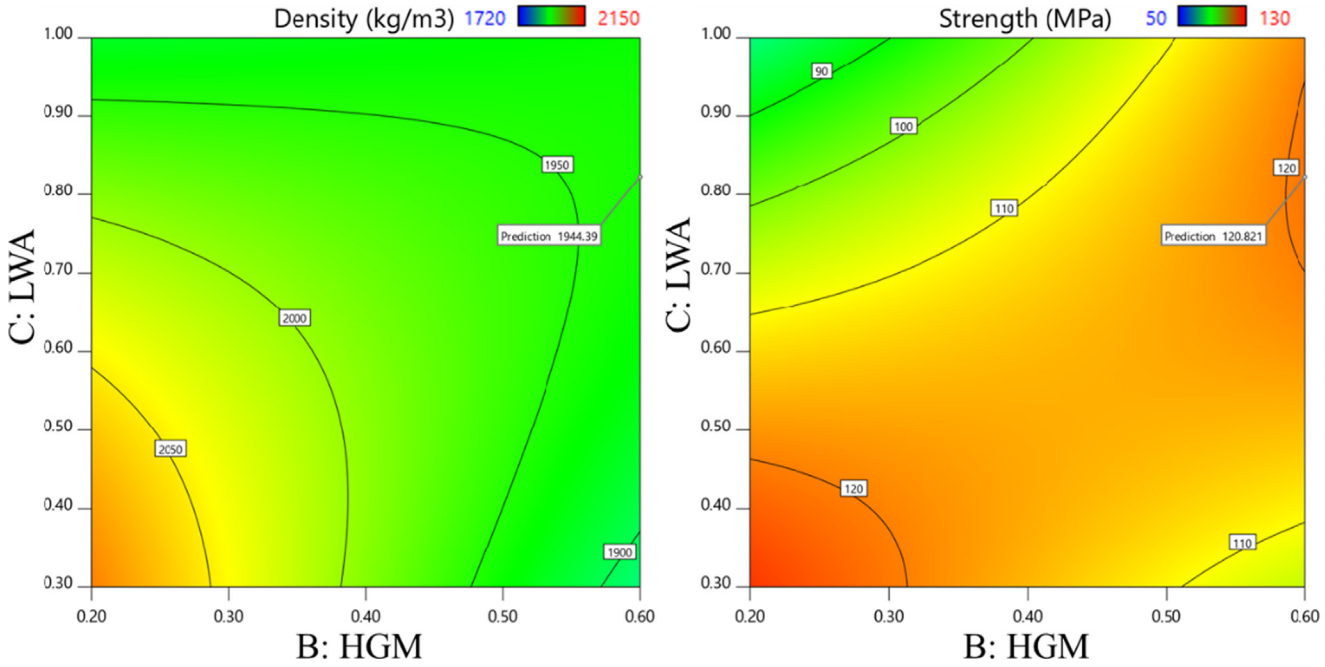

Fig. 7. Counter plot of optimization of L-UHPC mixture (OPC = 0.92).

Table 8
Experimental results of two randomly-selected proportions.

OPC	HGM	LWA	Density (kg/m^3)	Strength (MPa)
0.77	0.34	0.40	1982	114.0
0.84	0.60	0.85	1863	104.0

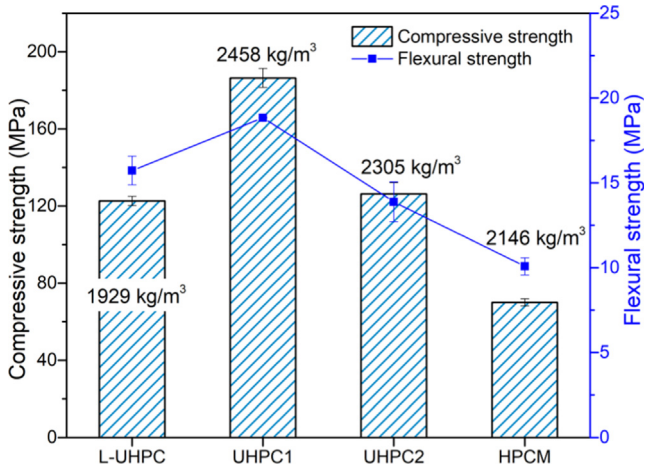

Fig. 8. Surface-dry density and mechanical properties of samples.

tance to the penetration of aggressive ions as compared to the UHPC1 with higher density. It is interesting to note that the L-UHPC seemed to have a slightly lower ion permeability than the UHPC2 with the same grade strength. This indicates that the good quality paste used in the L-UHPC played a positive role in the resistance of ion penetrability.

The water sorptivity was measured to determine the susceptibility of samples to the penetration of water, which is also an important index of the durability of concrete [84,85]. Fig. 11b shows the water sorptivity of the samples as a function of the square root of exposure time ($\sqrt{\text{day}}$). The progress of water sorptivity included two stages: initial water absorption rate (<12 h) and secondary water absorption rate (>24 h). In the initial stage, the water absorption rate of HPCM increased rapidly and the amount of water absorbed was much larger than the other samples. For UHPC samples, the UHPC2 had a higher water uptake than UHPC1. Within the first 12 h, the water absorption rate of L-UHPC was similar to that of UHPC1 but lower than that of UHPC2. During the second stage, the trends was similar to those in the initial period. The HPCM absorbed the largest amount of water and the UHPC1 absorbed the least. In particular, it is noted that the water absorption value of the L-UHPC prepared with HGM and LWA were lower than that of UHPC2 having a similar strength. As all the water absorption rates of samples correlated linearly with the square root of exposed time, the secondary rate of absorption can be calculated based on the least-square linear regression method (R^2 > 0.97). The obtained rates of water absorption are listed in Table 10.

As shown in Table 10, the rates of water sorptivity in the secondary stage were lower than those in the first stage. That is because the initial absorption was mainly controlled by the capillary suction of the larger pores on the surface, and the secondary sorptivity was primarily dominated by the tortuosity and interconnectivity of the smaller pores [86]. Irrespective of the age, the mixtures prepared with a higher *w*/*b* ratio showed a higher water sorption than those prepared with a lower *w*/*b* ratio. In the secondary stage, the HPCM/UHPC2 samples absorbed nearly two–three times as much water as the UHPC1 sample. The lower absorption of the lower *w*/*b* ratio mixture was also found in the study of Martys and Ferraris [87]. The low *w*/*b* ratio mixture could lead to reductions of pore size and interconnectivity of the larger capillary pores, which was thought to restrict the water diffusion and sorption. The refined pore characteristics of samples at a low *w*/*b* ratio will be supported by MIP results in Section 3.3.1. For the L-UHPC mixture, its sorptivity coefficients were slightly higher than the UHPC1, but the L-UHPC mixture absorbed less water than the UHPC2 and HPCM mixtures.

The L-UHPC sample seemed to perform differently from conventional lightweight concrete, which is vulnerable to infiltration

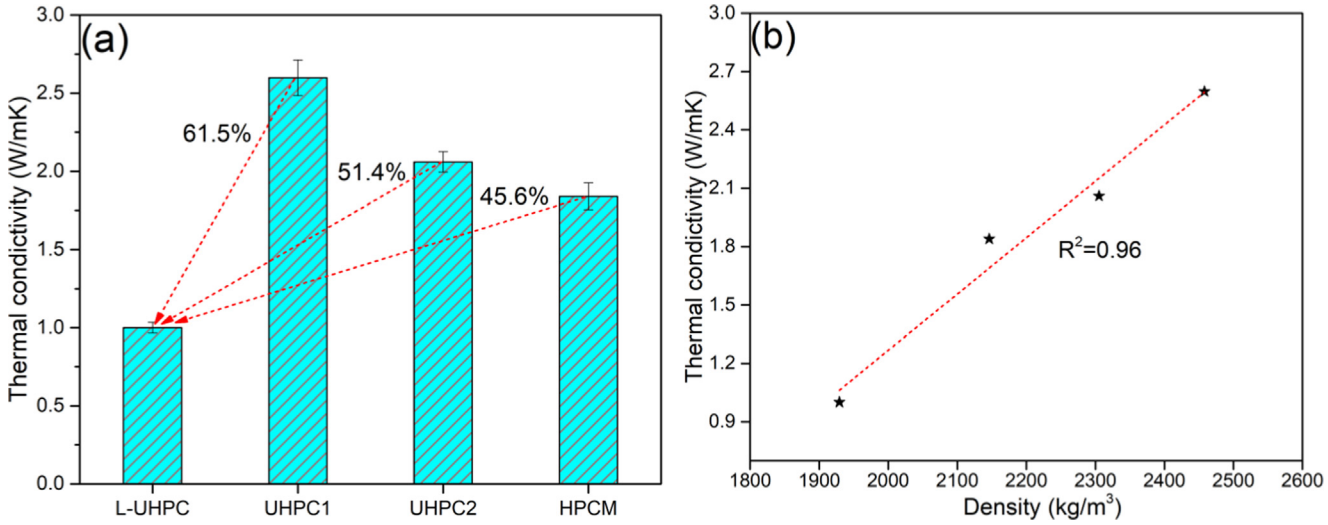

Fig. 9. Thermal conductivity of samples, (a) Thermal conductivity; (b) relation between the density and the thermal conductivity.

Table 9
Mix proportions of optimized L-UHPC, normal-weight UHPC and HPCM (kg/m^3).

Mix	OPC	HGM	SF	Water	SP	Fiber	LWA	RS	Flow (mm)
L-UHPC	758	66	246	165	34	117	509	/	210
UHPC2	907	/	246	280	10	117	/	1153	207
HPCM	907	/	246	458	4	117	/	1153	216

Note: The LWA containing water was pre-soaked for 24 h.

of deleterious ions and water. Although the L-UHPC contained a large quantity of voids induced by HGM and LWA, it still exhibited good resistance to chloride penetration and water absorption. The voids in the L-UHPC did not facilitate the penetration of ions and water. Several factors might account for the good performance: (i) the HGM and LWA were tightly packed by UHPC paste, which had a strong ability to resist the ingress of the deleterious substances due to its low porosity; (ii) the voids in the HGM and LWA were dispersed uniformly and isolated individually in the dense matrix, and thus they did not favor ions/water ingress via creating an interconnected pathway; (iii) the pozzolanic reactivities of the HGM and LWA contributed to the chemical reaction between them and the paste (as mentioned in Section 2.2), which was conducive to forming barriers against ions/water penetration through the HGM and LWA.

3.2.4. Autogenous and drying shrinkages

The volume changes of L-UHPC, UHPC and HPCM including autogenous and drying shrinkages are plotted in Fig. 12. Obviously, most of the autogenous shrinkage occurred within 24 h and the value decreased with increasing *w*/*b* ratio from UHPC1 to HPCM. These phenomena were also observed by Zhang et al. [88] in concrete at low *w*/*b* ratios. The UHPC mixtures exhibited very high autogenous shrinkage because of the very low water content, a large volume of fine powders, and the lack of coarse aggregates [16,89]. Autogenous shrinkage is the result of water withdrawal from the capillary pores due to the hydration reactions of the unhydrated cement [90], and thus capillary pressure is the driving force to generate self-desiccation (autogenous shrinkage). With the increase of water content in the mixture, the capillary pressure was reduced since the radius of meniscus in the capillary water was increased [91]. This effect was thought to be dominant for cement mixtures at early ages because early hydration was intensive and the tensile strength and tensile strain capacity of the matrix were relatively low.

As shown in Fig. 12a, very low autogenous shrinkage is observed for the L-UHPC in comparison with UHPC mixtures. This is explained by water absorbed by the LWA contributed to the internal curing of cement hydration, which mitigated the self-desiccation of the UHPC paste. The water absorption of the LWA was lower compared to that of conventional large-sized LWA, but the internal curing effect would still be anticipated. Liu and Wei [59] also incorporated the pre-wetted porous aggregates (a similar 24-h water absorption to the LWA in this study) into UHPC and found the high-efficient internal curing and significant reduction in the autogenous shrinkage. The stored water in the LWA was gradually released into the system to increase the internal moisture so as to reduce the capillary stress and autogenous shrinkage [92]. The incorporation of pre-saturated LWA has been reported to be capable of reducing the autogenous shrinkage of normal cement concrete and UHPC in other studies [93–95]. It is interesting to note that transitory expansions were observed before 24 h in the L-UHPC and UHPC mixtures. In the low *w*/*b* cement mixtures, the system was consolidated rapidly by calcium silicate hydrate (C-S-H) and other hydrates to form a dense packing matrix, and the very high ionic concentration and rapid supersaturation took place in the liquid–solid system to initiate a faster precipitation of hydration products. Therefore, at the very early age, the formation of large-sized portlandite and ettringite crystals might contribute to the expansive deformations due to the low stiffness of the matrix. This interpretation is in agreement with the work of Baroghel-Bouny et al. [96]. Furthermore, the slow release of the absorbed water in the LWA could promote the formation of additional C-S-H, which locally increased the solid volume surrounding the aggregates. The expansion phenomena were also found in other UHPC systems [20,97]. Nevertheless, the mechanisms of the swelling behavior in the UHPC should be further elucidated.

At the later age, when water moved out from the samples in a low humidity condition, volumetric contractions took place. Fig. 12b presents low drying shrinkage values of L-UHPC and UHPC1, and the value increased with a higher *w*/*b* ratio. These results are contrary to those of the autogenous shrinkage. The reason is that: during drying shrinkage measurements which occurred at a later age, the hydrating matrix had already developed a certain rigidity, and therefore the volume change of the samples was mainly due to the water loss in the drying environment rather than contraction induced by hydration (internal drying). The lower drying shrinkage values of L-UHPC and UHPC1 were due to: (i) the rigid skeleton of hardened matrix with an ultra high strength was able to restrain the deformation due to moisture evaporation [90]; (ii) the small amount of water in the matrix did not allow much water loss. On the contrary, for the mixtures prepared with a high water content, the volume change was higher. Therefore, although the HPCM had a low autogenous shrinkage value, the higher drying deformation occurred after a longer exposure time. It should be noted that the large quantity of voids in the L-UHPC did not have a negative effect on drying deflection. This means that the rigid structure of the paste matrix in such concrete (to be discussed in Section 3.3.3) could counteract the lower elastic modulus of the voids and LWA and reduce the drying shrinkage.

3.3. Microstructure analyses

3.3.1. Pore structure

The pore structures of L-UHPC, UHPC and HPCM determined by MIP are illustrated in Fig. 13. It is clear to observe that the total porosity of the mixtures was reduced largely with the decrease of *w*/*b* ratio. Only 1.58% of connective pores was detected in UHPC1, which is in agreement with its highest density and mechanical properties. The HPCM showed the highest porosity due to the highest water content in the mixture, thus the density and the strength were corresponding the lowest among the normal weight mixtures. This is also the reason for its highest permeability and water absorption. As the L-UHPC was prepared with a large amount of HGM and LWA, its porosity (6.68%) was higher than that of UHPC2 (4.66%). Hence, the L-UHPC had a much lower density than the UHPC2. However, although the MIP results indicated that L-UHPC had a denser microstructure than the HPCM (6.68% vs. 13.13%), the density of former was still lower than that of the latter. This implies that a large quantity of the voids in the L-UHPC

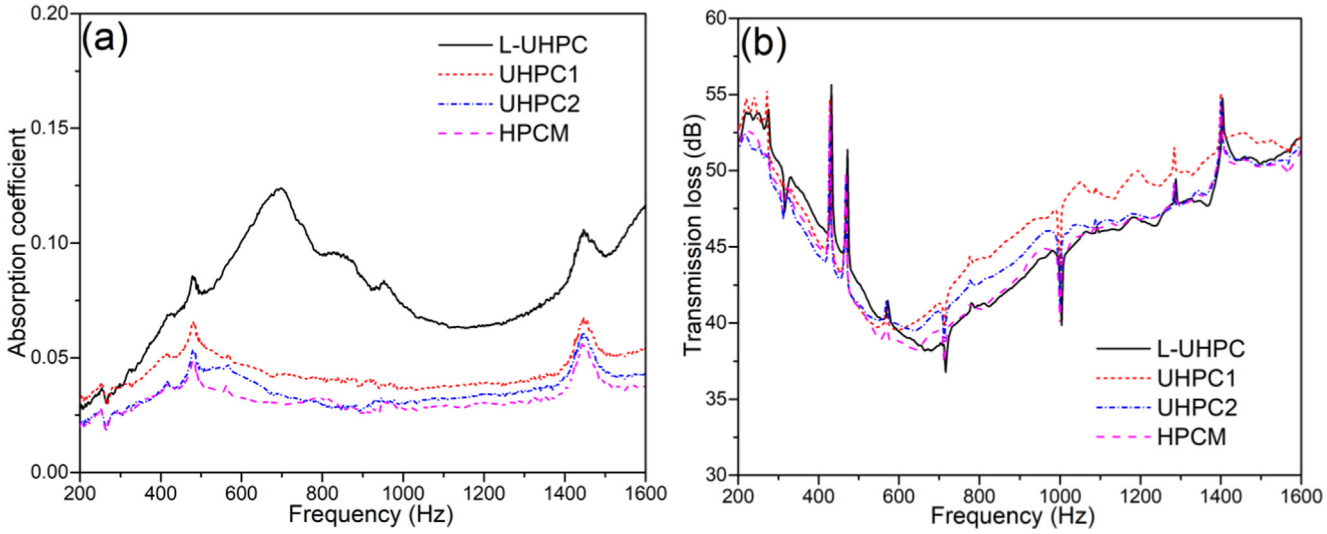

Fig. 10. Acoustic properties of samples, (a) absorption spectra of sound; (b) transmission loss of sound.

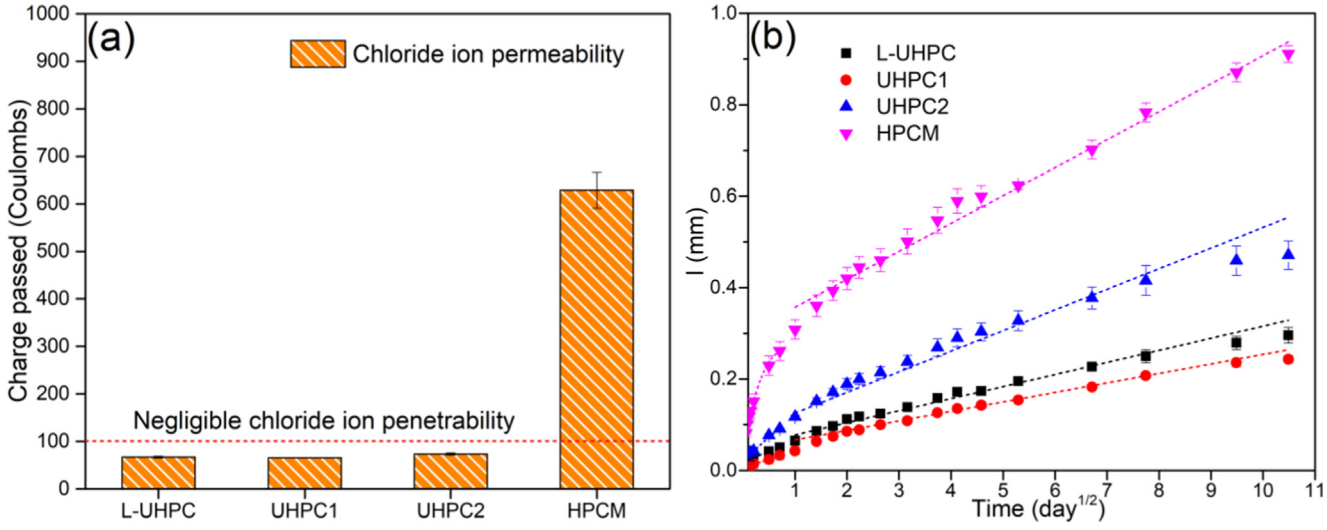

Fig. 11. Ion permeability (a) and water sorptivity (b) of samples.

Table 10
Rate of water absorption of L-UHPC, UHPC and HPCM (mm/day$^{1/2}$).

Mix	Rate of water absorption	
	Initial stage	Secondary stage
L-UHPC	4.5×10^{-2}	2.4×10^{-2}
UHPC1	4.0×10^{-2}	2.1×10^{-2}
UHPC2	9.9×10^{-2}	4.5×10^{-2}
HPCM	/	6.1×10^{-2}

Note: The HPCM in the initial absorption stage showed a systematic curvature rather than a linear relationship, thus its initial rate of absorption cannot be determined.

were enclosed and disconnected, which could not be characterized by MIP. Despite the higher porosity of L-UHPC, its mechanical properties were still comparable to those of UHPC2 with a lower porosity. The possible reason is that the effect of the higher paste stiffness in the L-UHPC surpassed that of the voids, contributing to the better overall strength of the matrix (to be discussed in Section 3.3.3).

Fig. 13b shows the pore size distributions of the samples. Obviously, the HPCM had more large pores and also a large number of fine pores (<50 μm). The pores detected by MIP were interconnected, and thus the large volumes of voids and capillary pores contributed to the poorer resistances to ions and water infiltrations. With the decrease of *w*/*b* ratio, the quantity of capillary pores was reduced, and hence a lower permeability and water penetration was achieved. For the L-UHPC, it is interesting to note that the amount of gel pore (<10 nm) was significantly increased as compared to UHPC mixtures (in insert figure). As the sizes of voids in the HGM and the LWA were mainly larger than 100 nm, their influences on the results were neglected. The gel pore is the intrinsic porosity of C-S-H gel [73], it is thus deduced that the formation of C-S-H was increased. There were several contributors for the increased amount of gel pore: (i) the internal curing of pre-soaked LWA facilitated further hydration of the unhydrated cement to form more C-S-H gel; (ii) the pozzolanic reactions of HGM and LWA contributed to additional C-S-H; (iii) the released water from LWA enabled the pozzolanic reaction of the remaining silica fume to densify the matrix. These pozzolanic reactions were

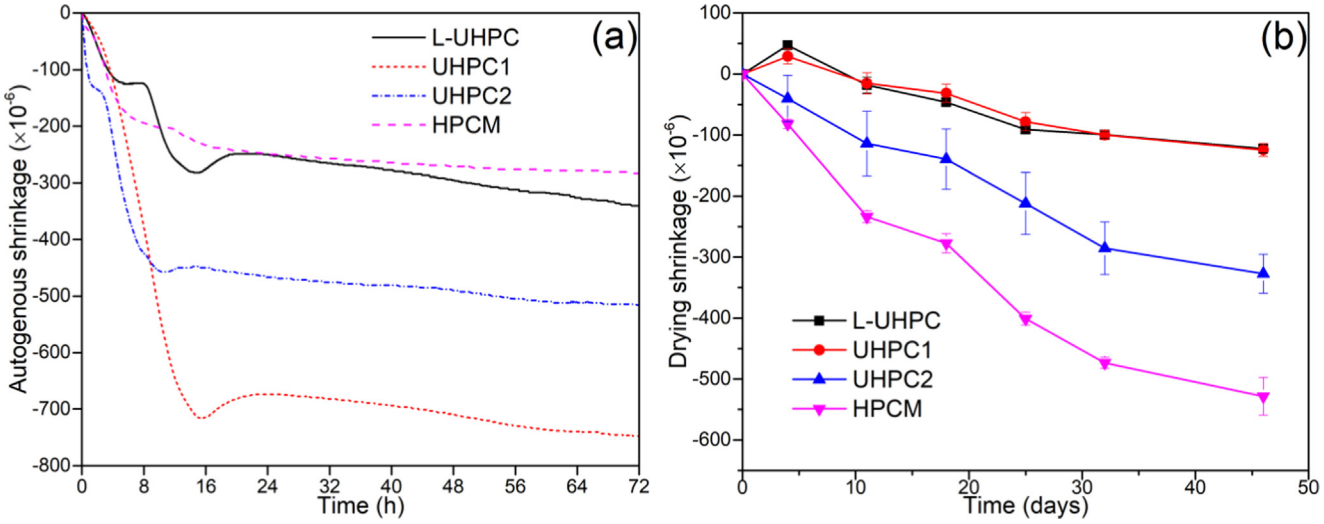

Fig. 12. Shrinkages of samples, (a) autogenous shrinkage and (b) drying shrinkage.

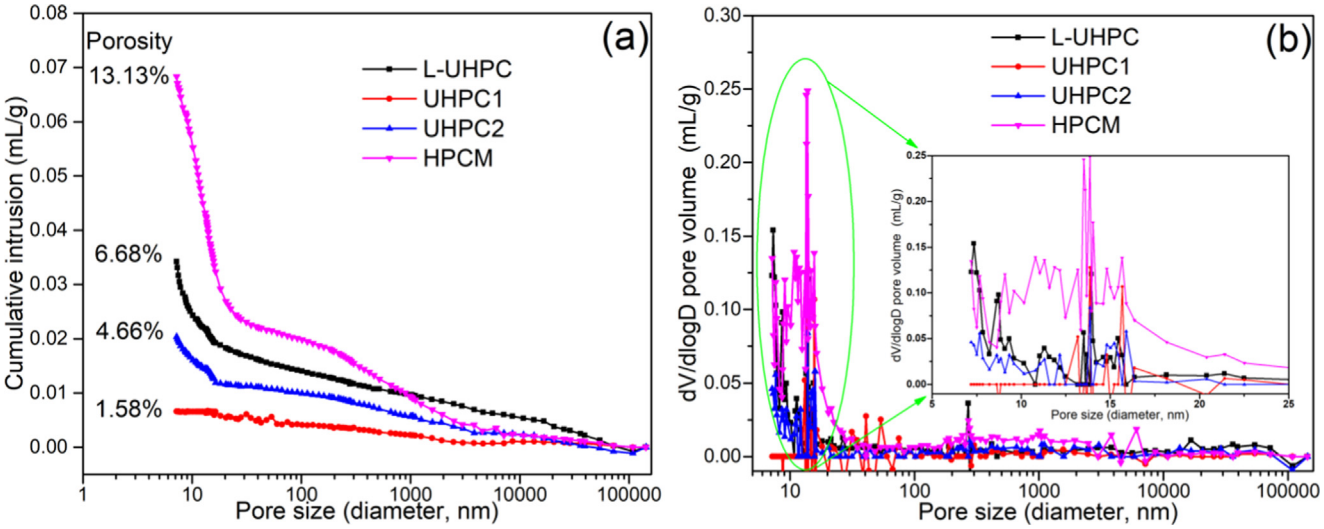

Fig. 13. Pore structure of samples, (a) cumulative intrusion; (b) pore size distribution.

conducive to strengthening the paste matrix and partly counteract the weak zones of the lightweight materials (i.e. HGM and LWA). This explanation is consistent with the ultra high strength and good durability of L-UHPC.

3.3.2. Morphological observation

Fig. 14 presents the morphologies of UHPC1 and L-UHPC samples by BSE observations. In Fig. 14a and b, a large number of unreacted cement particles were observed around the RS in the UHPC1. A clear boundary between the paste and the RS aggregates was observed. By means of EDX analysis, the bright and bigger particles were unhydrated clinker phases with relatively low reactivities. The low water content in the UHPC system was responsible for the cement-superfluous phenomenon. Fig. 14c shows the porous LWA embedded in the L-UHPC matrix and many unreacted cement particles could be also seen in the matrix due to the low *w*/*b* ratio. Besides, the incorporation of the hollow HGM brought a number of cavities into the paste matrix. The presence of these two void-containing materials was the reason of weight reduction. The LWA and its boundary could be identified by elemental mapping (Fig. 14e), which also indicates the unreacted clinker phases (yellower Ca-rich particles) surrounding the LWA. It is further found that the smaller size unhydrated cement particles were located in the immediate vicinity of the LWA, while the larger size unhydrated cement particles were located further from the LWA. This phenomenon might be the result of the internal curing effect of the pre-wetted LWA. In addition, it is noted that the bonding between the paste and the LWA provided an interlock, where the paste penetrated into the open-pores of LWA surface to intensify the bonding with the paste matrix [98]. A closer observation of Fig. 14d (magnified area of Fig. 14c) shows some corroded HGM particles in the paste matrix. This indicates the interactions between the shell of HGM and the surrounding alkaline hydration products. The result of the pozzolanic reactivity of HGM in Fig. 2 supports this observation. However, the interior surface of HGM seemed to be smooth, which implies the limited reaction of the exterior surface and the intact shell structure of the HGM. This observation explains the low porosity recorded for the L-UHPC as

the voids in the HGM were closed pores and enclosed by shell. On the other hand, the shell-paste interface would be reinforced by the additional reaction products (to be discussed in Section 4).

Fig. 14f shows another LWA particle in the L-UHPC. Large pores could be found in the LWA, which would store water for internal curing. Several big pores of the LWA were filled with the paste (aqua enclosure). This partly compensated for the weak strength of LWA. EDX point analysis was performed in the surrounding or interior areas of LWA, and the elemental composition results are listed in Table 11. The very low Ca/Si or Ca/(Si + Al) ratios of these areas (mostly < 1.0) suggest that the pozzolanic reaction of LWA (rich in Si and Al) was probably involved in the formation of hydrates around LWA. The internal curing effect of pre-soaked LWA was expected to facilitate this pozzolanic reaction, which improved the interfacial transition zone (ITZ) between the LWA and the cementitious matrix. The formation of additional C-S-H

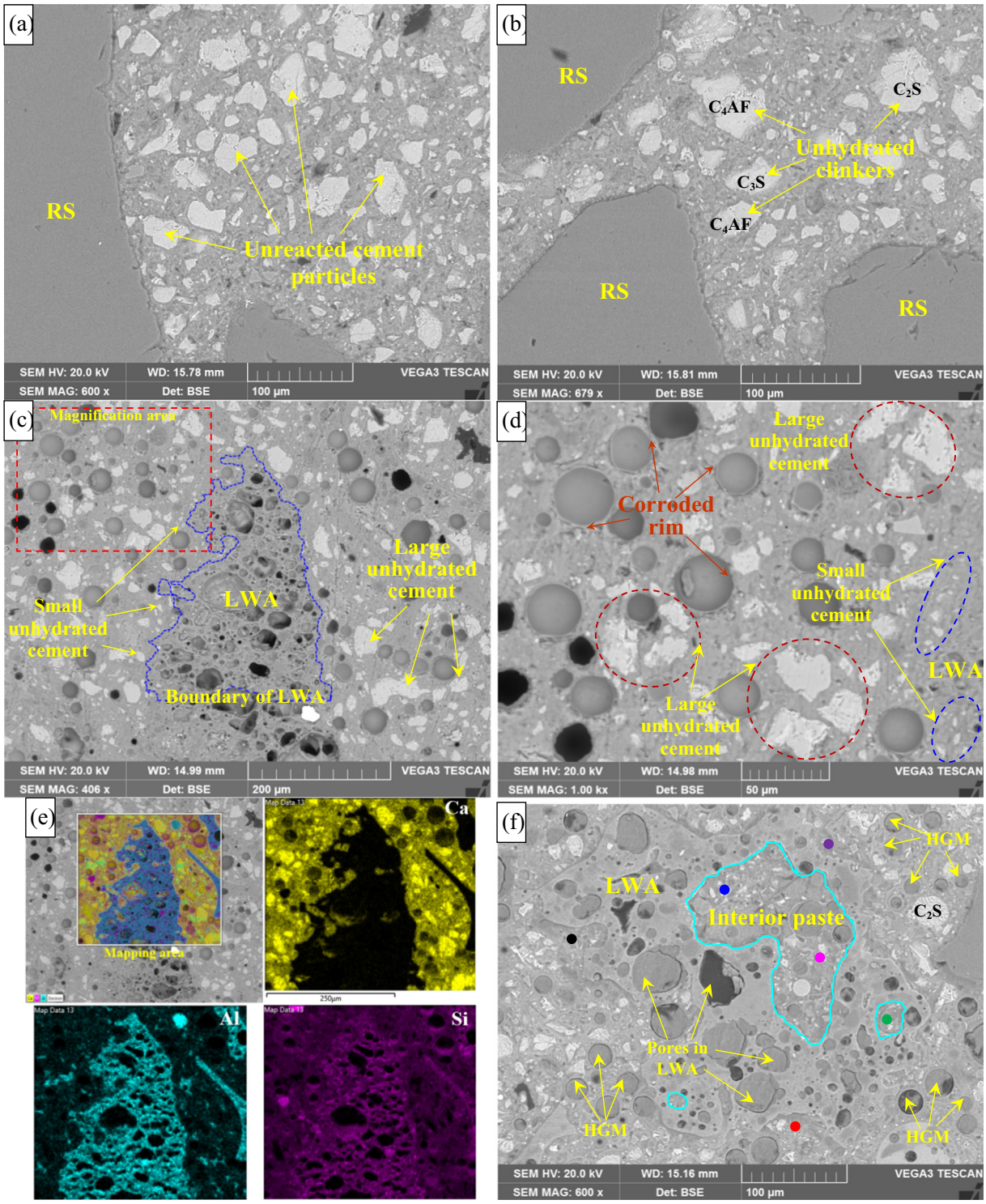

Fig. 14. BSE images of UHPC1 and L-UHPC, (a, b) UHPC1; (c, d) L-UHPC; (e) Elemental mapping of c; (f) EDX points in L-UHPC. Note: C_3S: Alite phase, C_2S: Belite phase, C_4AF: Tetra-calcium aluminoferrite phase.

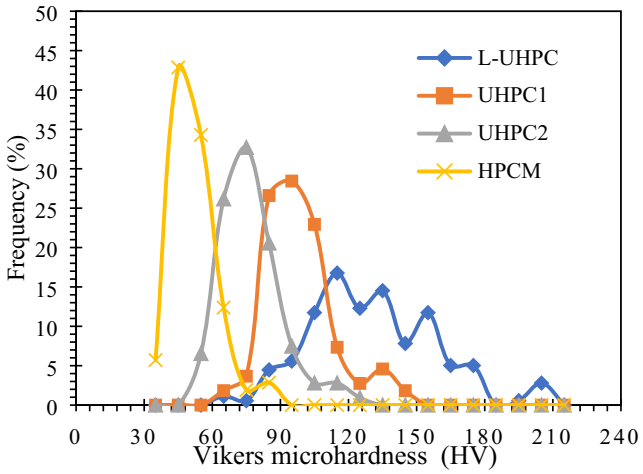

Fig. 15. Frequency distributions of microhardness of cement paste in samples.

could reinforce the LWA and form a barrier against the infiltration of deleterious substances and the local stress exerting on the LWA.

3.3.3. Microhardness of cement paste

The Vickers microhardness was determined to understand the stiffness of paste matrix in the samples. The higher the microhardness value, the denser is the microstructure of bulk paste. Based on more than 100 points for one mixture, the frequency distributions of microhardness values of cement paste in L-UHPC, UHPC and HPCM are shown in Fig. 15. It shows that the main peak of the microhardness profiles shifted from low value to high value from the HPCM to UHPC1. The microhardness value ranges corresponding to the highest frequency of HPCM, UHPC1 and UHPC2 were 40–50 HV, 70–80 HV and 90–100 HV, respectively. Therefore, when the *w*/*b* ratio was reduced, the rigidity of the paste matrix was increased considerably. The lower porosity of the mixture at a lower *w*/*b* ratio resulted in the higher microhardness and the denser microstructure. The higher stiffness of the paste matrix was also responsible for improving the mechanical properties of the whole samples [99].

As can be seen in Fig. 15, the microhardness data show a broad frequency distribution associated with the bulk paste of L-UHPC. This implies a more heterogeneous microstructure in the L-UHPC matrix. However, the more frequent occurring microhardness range was 110–120 HV, which was much higher than those of UHPC and HPCM mixtures. Besides, the average microhardness value was 130.1 HV, 98.8 HV, 77.5 HV and 52.5 HV, corresponding to L-UHPC, UHPC1, UHPC2 and HPCM, respectively. These results reveal that the bulk paste in the L-UHPC had a denser microstructure than their counterparts in the UHPC and HPCM mixtures. The internal curing provided by LWA and the chemical reactions between the LWA/HGM and the cement paste were believed to enhance the micromechanical properties of the paste matrix. A recent study [55] also reported the increased micromechanical properties at the interfacial zone of LWA, the internal curing and Al dissolution from LWA were thought to densify the interfacial matrix. As a consequence, due to the reinforced rigidity of paste matrix, the L-UHPC exhibited an ultra high strength and excellent durability properties although it contained a large volume of voids.

4. Discussion

4.1. Effectiveness of CCD in the design of L-UHPC

As discussed above, the CCD model was able to predict the density and strength of L-UHPC. By means of the CCD model, an optimized L-UHPC with ultra high strength and low density was successfully produced. More importantly, the excellent performance in terms of durability properties indicates the effectiveness of the CCD in the design of L-UHPC. By using CCD, the optimized mixture was a result the integration of different factors, including good compaction of the constituents, physicochemical reactions between different phases, and homogeneity of mixture etc. One concern of producing LWC is the high susceptibility of segregation due to the different densities of the constitutes, which would affect the mechanical and durability properties of concrete [100]. Hence, an X-ray CT was employed to examine the distributions of LWA and fibers in the matrix with a view to validating the homogeneity of L-UHPC designed by CCD method. The 3D images obtained by X-ray CT are shown in Fig. 16. From Fig. 16b and c, the steel fibers were arrayed randomly and uniformly in the matrix, which means the heavy fibers were not segregated to the bottom of the samples. The uniform distribution of fibers was attributed to the good flowability of the optimized mixture, which was further a result of the integration of multi-ingredients and interaction between the experimental variables. Hence, the homogenous dispersion of fibers was attributed both to the good flowability and effective design.

To observe the possible segregation of LWA in the L-UHPC, 2D images of the cross-sections (upper, middle and lower) and the longitudinal-sections (front, middle and back) of the sample were extracted and presented in Fig. 16(d, e, f) and (g, h, i), respectively. The fine LWA particles were dispersed evenly on each of the cross-section. From three longitudinal-sections, the LWA particles were also observed to locate in the bottom of L-UHPC and the LWA did not aggregate in the upper parts of the sample due to floatation. Therefore, it is believed that the low density LWA was able to distribute uniformly in the L-UHPC matrix. The random distribution of fibers contributed to the high mechanical properties, especially in improving the flexural strength. The uniform distribution of LWA was conducive to lowering the thermal conductivity and shrinkages owing to the extensive coverage of voids and provision of internal curing. The CT results indicate that CCD method was effective in designing a homogenous L-UHPC.

4.2. Roles of HGM and LWA in L-UHPC

The excellent performance of L-UHPC was primarily dependent on the characteristic of the paste matrix and the roles of the light-

Table 11
Element compositions of EDX points in Fig. 14f (Atomic %).

Element	Pink point	Blue point	Green point	Red point	Black point	Purpure point
O	69.5	63.3	71.4	69.3	64.5	68.6
Al	1.6	2.1	5.8	7.1	4.7	4.9
Si	13.5	19.1	11.0	11.0	23.1	13.4
Ca	13.6	14.2	9.8	10.4	6.6	11.8
Ca/Si	1.01	0.74	0.89	0.95	0.29	0.88
Ca/(Si + Al)	0.90	0.67	0.58	0.57	0.24	0.64

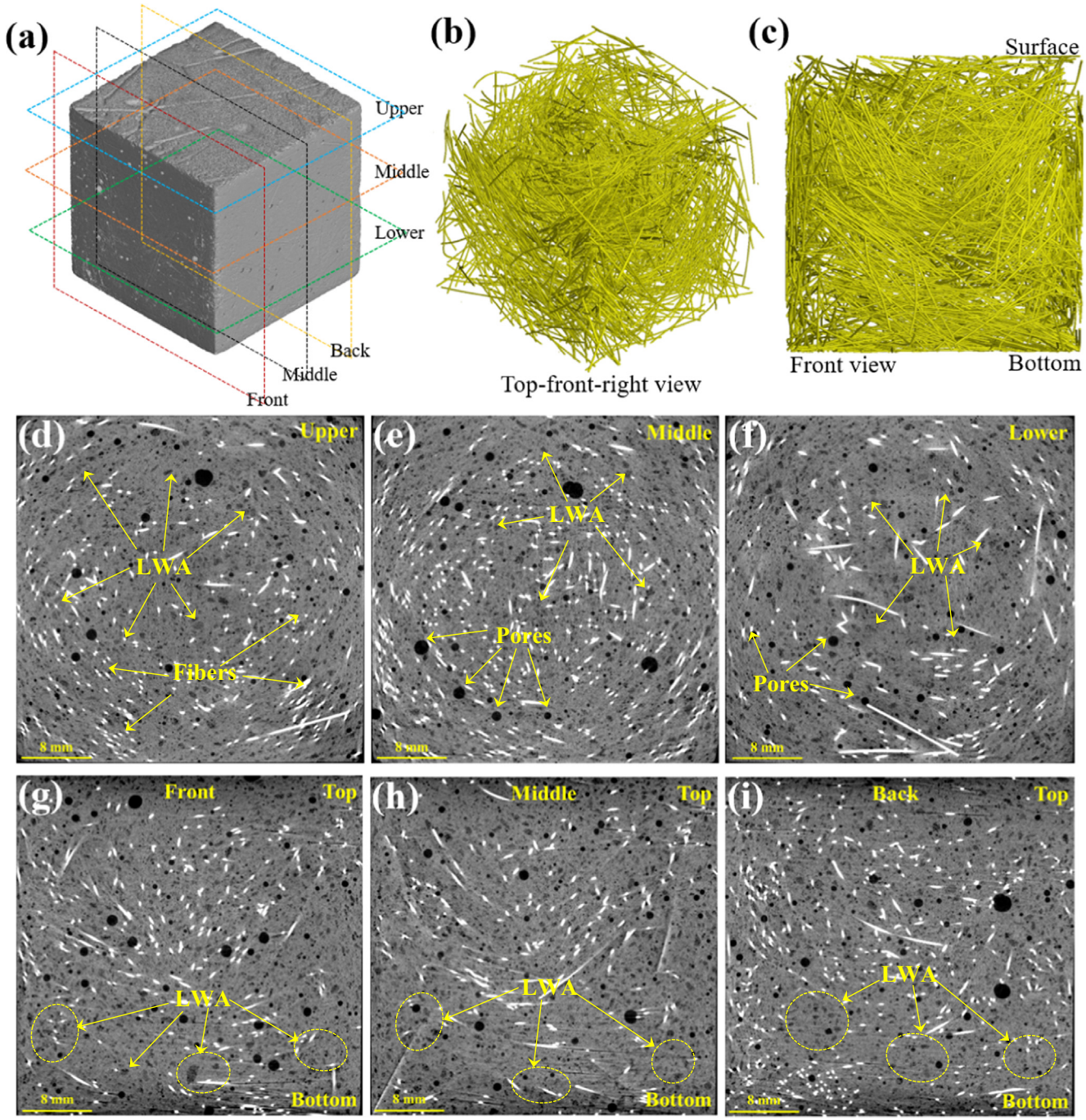

Fig. 16. Distributions of steel fiber and LWA determined by X-ray CT, (a) L-UHPC sample and section profiles; (b) top-front-right view of steel fibers; (c) front view of steel fibers; (d, e, f) cross-sections: Upper, Middle and Lower; (g, h, i) longitudinal-sections: Front, Middle and Back.

weight materials used in this study. The good quality UHPC paste played a dominant role in governing the durability properties of L-UHPC. Besides, as the strength of the LWC is sensitive to porosity, the roles of HGM and LWA were also of great importance in controlling the performance of L-UHPC.

As indicated by the CCD analysis, the compressive strength of the L-UHPC seemed to increase with the increasing amount of HGM (Fig. 6). This result means that, within a specific amount of HGM usage, the amount of HGM had insignificant effect on the strength of the L-UHPC. Previous studies [101–103] also reported that the use of HGM below a specified volume could slightly increase the mechanical properties of the concrete mixtures. Besides being light weight, the high-stiff shell and micro-size of HGM also were conducive to enhancing the fracture energy of the L-UHPC when stresses were exerted on the HGM. Moreover, the non-absorbent characteristic, smooth surface and spherical shapes of HGM also facilitated the compaction and homogeneity of the mixture due to its lubricating effect. As reported, the introduction of HGM could reduce entrapped air contents [101] and improve the workability [104] of concrete mixtures. As shown in Fig. 17a, most of HGM particles were damaged across the shell of the HGM sphere rather than through the interface between the HGM and the matrix. Also, Fig. 17b presents an etched and rough surface of HGM found in the aged sample which was very different

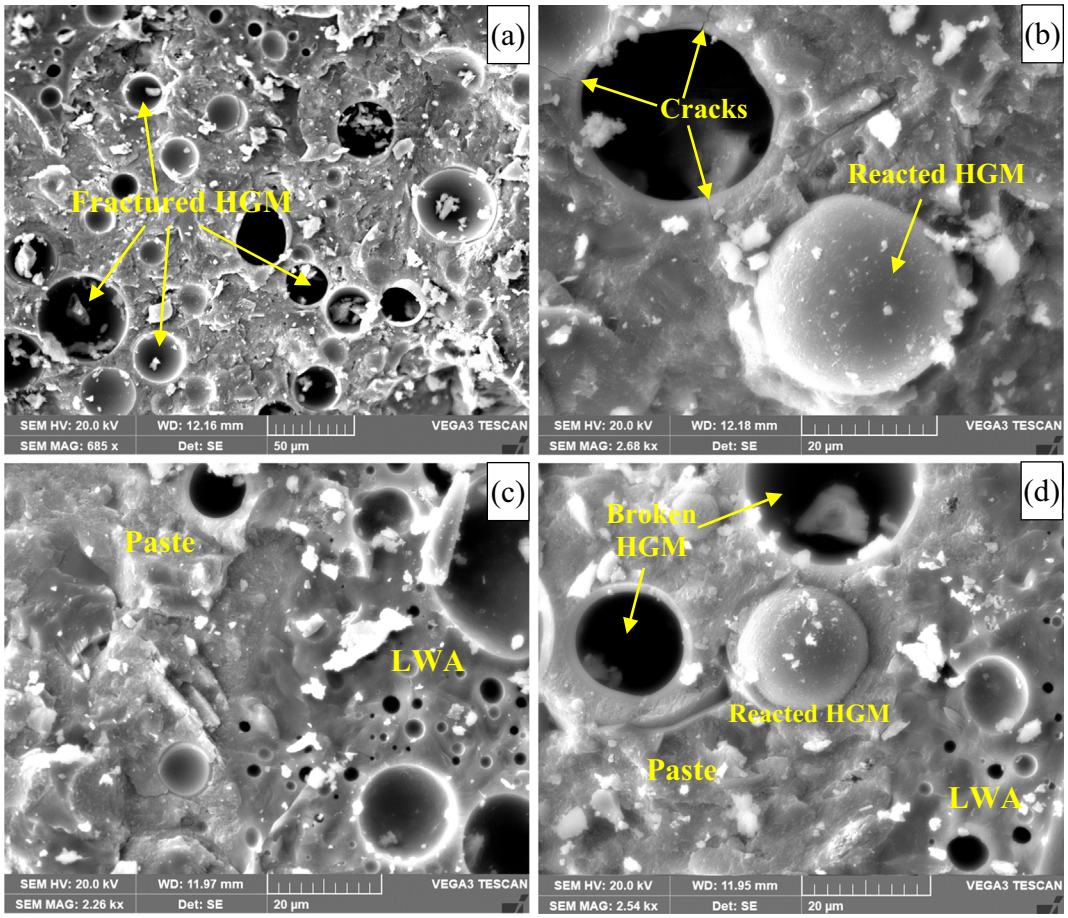

Fig. 17. SEM images of the fractured L-UHPC, (a, b) failure of HGM; (c, d) interface of paste-LWA.

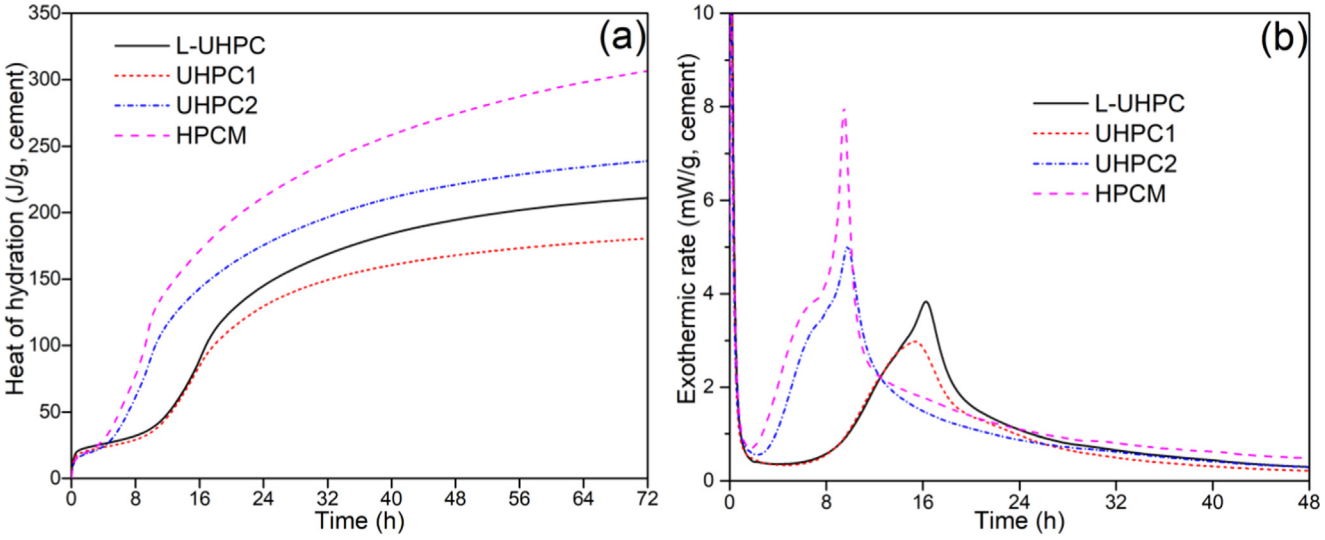

Fig. 18. Heat release of per gram of cement in samples, (a) cumulative heat and (b) rate of heat flow.

from that seen in the unreacted HGM (see Fig. 3). These results suggest a high interfacial toughness of the HGM-paste owing to the additional C-S-H formed on the shell of HGM, which impeded the propagation of cracks across the interface. Similarly, a recent study [105] found the same failure mode of HGM in a steam cured oil-well cement. Therefore, the chemical reaction between the HGM and the surrounding alkaline hydrates contributed to the bonding of HGM and paste, which was able to reinforce the thin shell and increase the load bearing capacity of HGM.

Since the HGM mainly composed of amorphous silica, the potential issue arises from the use of HGM is the alkali-silica-reaction (ASR) concern. However, it is believed that the ASR risk

will not be provoked in the L-UHPC system. The reasons include: (i) similar to micro-sized glass powder [106], the HGM acted as a pozzolanic material rather than aggregate role, thus pozzolanic reaction occurred instead of ASR; (ii) the presence of silica fume in the mixture would effectively suppress the potential ASR [107]; (iii) the HGM had porous structure, the interior void would accommodate the ASR gel if the thermal expansion was triggered; (iv) little water content inside the L-UHPC did not provide sufficient water to evoke the ASR. A recent work [108] also confirmed the safe use of HGM in cementitious mixture, the explanation was that the reservoir space of HGM could take in the internal stress and ASR expansion.

In this study, pre-soaked LWA was used as a fine aggregate and an internal curing agent for the production of L-UHPC. The morphology of LWA indicated that many open pores were embedded in the matrix of LWA (Fig. 3). These pores could act as water reservoirs to supply water to their surrounding paste for internal curing. Therefore, the water release from the LWA was thought to result in the mitigation of the self-desiccation of L-UHPC (Fig. 12). Besides its ability to reduce autogenous and drying shrinkage, the desorbed water from the LWA might be able to promote the further hydration of unhydrated cement and the secondary pozzolanic reaction of unreacted SF. To validate this proposition, heat of hydration of the mixtures was measured by isothermal calorimetry (Calmetrix I-Cal 4000) and the results are plotted in Fig. 18. As compared to UHPC1, the L-UHPC prepared with the same w/b ratio released more heat within 3 days. The higher heat flow rate of L-UHPC (Fig. 18b) resulted in higher heat output. The enhancement of the hydration means that more hydrates were produced which would further strengthen the paste matrix surrounding the LWA. Hence, the higher microhardness of paste matrix in the L-UHPC was attained (see Section 3.3.3). The UHPC2 and HPCM mixtures showed earlier exothermic peaks and higher total amount of heat due to their higher water contents and the less amounts of water reducing agent used. Recently, several studies also suggested that the use of a small volume of pre-saturated LWA could increase the mechanical properties of UHPC [92,95,109]. Such improvement implies that the internal curing effect derived from pre-soaked LWA could partly compensate the negative effect of the porous LWA.

The other factor contributing to the ultra high strength was the use of small size LWA. The smaller size of LWA would have a higher ability to resist stress or ion infiltration because the fine LWA contained more small isolated pores rather than large connected pores [110]. Also, for a given amount of LWA, the smaller size of LWA led to closer distances between the aggregates [110], thus the extensive distribution of small-sized LWA allowed the absorbed water to permeate to the paste between the nearest aggregate, which showed a higher effectiveness in curing the surrounding matrix in comparison with coarser LWA [111]. The paste could also penetrate into the open-pores in the LWA to reinforce the interface strength of LWA (see Section 3.3.2). Furthermore, the high pozzolanic reactivity of LWA under hydrothermal curing and interlocking bonding of LWA-paste intensified the rim of LWA and the vicinal paste matrix (Fig. 17(c and d)). The above physicochemical interactions might account for the insignificant loss of strength when the amount of LWA was below a specified volume (see Fig. 6).

5. Conclusion

This study developed a mix design method to produce a lightweight ultra high-performance aggregate concrete (L-UHPC) with ultra high strength, low density and excellent durability. The combined use of a high strength lightweight pozzolanic material (i.e. HGM) and a small-sized lightweight fine aggregate (i.e. LWA) was effective to produce this L-UHPC. The following conclusions from the experimental investigation can be drawn:

(i) The analysis of variance indicated the good applicability and reliability of the response surface quadratic model for the prediction of density and strength. The use of the Central Composite Design method was feasible to design a homogenous L-UHPC with ultra high strength and low density. The incorporation of HGM effectively reduced the density of L-UHPC without loss of strength.

(ii) The optimized mixture had a compressive strength of 123 MPa and surface-dry density of 1929 kg/m^3, which could be qualified as a lightweight UHPC. The combined use of lightweight HGM as a pozzolanic material and LWA as a fine aggregate was effective in reducing density and attaining ultra high strength. The structural efficiency of L-UHPC (63.6 kN·m/kg) was much higher than those of current high strength/performance lightweight concrete.

(iii) The L-UHPC had about half of the thermal conductivity value of conventional UHPC mixtures. The combined use of HGM and LWA in the L-UHPC significantly enhanced the sound absorption due to the incorporation of large quantities of acoustical cavities.

(iv) The resistance to ion penetrability of L-UHPC was excellent, which was comparable to traditional UHPC mixtures. Also, the L-UHPC had a lower rate of water absorption than the UHPC at the same grade strength. The voids associated with the HGM and the LWA did not facilitate the ions/water penetration in the L-UHPC.

(v) Very low autogenous and drying shrinkages were found for the L-UHPC in comparison with the UHPC and HPCM mixtures. The internal curing provided by the pre-soaked LWA was beneficial to mitigating the self-desiccation of the UHPC paste, and the rigid matrix and low water content resulted in low drying shrinkage.

(vi) The internal curing provided by LWA promoted the further hydration of unreacted cement and pozzolanic reactions of LWA and HGM. The paste of L-UHPC had a high microhardness value, which partly counteracted the defects induced by the HGM and LWA, and contributed to the high strength of the overall matrix. The physicochemical interactions of UHPC system, high strength micro-sized HGM and pre-soaked fine LWA made contributions to produce an L-UHPC with excellent performances.

Declaration of Competing Interest

The authors declare that they have no known competing financial interests or personal relationships that could have appeared to influence the work reported in this paper.

Acknowledgement

The authors gratefully acknowledge the financial support of The Hong Kong Polytechnic University through RCRE, Hong Kong Innovation and Technology Fund (PRP/044/21FX) and Teaching Postgraduate Studentship Scheme. The technical assistances of Dr. Ting Fai Kong and Ms. Emily Fung in the X-ray CT and acoustic properties tests are gratefully acknowledged. Thanks are also due to Ms. Dorothy, Chan for her assistance in the SEM observation.

References

[1] L.A. Sbia, A. Peyvandi, J. Lu, S. Abideen, R.R. Weerasiri, A.M. Balachandra, P. Soroushian, Production methods for reliable construction of ultra-high-

performance concrete (UHPC) structures, Mater. Struct. 50 (1) (2017), https://doi.org/10.1617/s11527-016-0887-4.
[2] N.A. Soliman, A. Tagnit-Hamou, Using particle packing and statistical approach to optimize eco-efficient ultra-high-performance concrete, ACI Mater. J. 114 (2017).
[3] J. Van Der Putten, J. Dils, P. Minne, V. Boel, G. De Schutter, Determination of packing profiles for the verification of the compressible packing model in case of UHPC pastes, Mater. Struct. 50 (2) (2017), https://doi.org/10.1617/s11527-016-0986-2.
[4] Y. Shi, G. Long, X. Zen, Y. Xie, T. Shang, Design of binder system of eco-efficient UHPC based on physical packing and chemical effect optimization, Constr. Build. Mater. 274 (2021) 121382.
[5] A. Arora, A. Almujaddidi, F. Kianmofrad, B. Mobasher, N. Neithalath, Material design of economical ultra-high performance concrete (UHPC) and evaluation of their properties, Cem. Concr. Compos. 104 (2019) 103346.
[6] X. Wang, R. Yu, Q. Song, Z. Shui, Z. Liu, S. Wu, D. Hou, Optimized design of ultra-high performance concrete (UHPC) with a high wet packing density, Cem. Concr. Res. 126 (2019) 105921.
[7] Y. Wu, J.-Y. Wang, P.J.M. Monteiro, M.-H. Zhang, Development of ultra-lightweight cement composites with low thermal conductivity and high specific strength for energy efficient buildings, Constr. Build. Mater. 87 (2015) 100–112.
[8] Q.L. Yu, P. Spiesz, H.J.H. Brouwers, Ultra-lightweight concrete: Conceptual design and performance evaluation, Cem. Concr. Compos. 61 (2015) 18–28.
[9] S.K. Adhikary, Ž. Rudžionis, D. Vaičiukynienė, Development of flowable ultra-lightweight concrete using expanded glass aggregate, silica aerogel, and prefabricated plastic bubbles, J. Build. Eng. 31 (2020) 101399.
[10] Q. Zeng, T. Mao, H. Li, Y. Peng, Thermally insulating lightweight cement-based composites incorporating glass beads and nano-silica aerogels for sustainably energy-saving buildings, Energy Build. 174 (2018) 97–110.
[11] H. Du, Properties of ultra-lightweight cement composites with nano-silica, Constr. Build. Mater. 199 (2019) 696–704.
[12] A. Raj, D. Sathyan, K.M. Mini, Physical and functional characteristics of foam concrete: A review, Constr. Build. Mater. 221 (2019) 787–799.
[13] M. Zhou, W. Lu, J. Song, G.C. Lee, Application of Ultra-High Performance Concrete in bridge engineering, Constr. Build. Mater. 186 (2018) 1256–1267.
[14] Y.H.M. Amran, N. Farzadnia, A.A. Abang Ali, Properties and applications of foamed concrete: a review, Constr. Build. Mater. 101 (2015) 990–1005.
[15] L. Yang, C. Shi, Z. Wu, Mitigation techniques for autogenous shrinkage of ultra-high-performance concrete – a review, Compos. B Eng. 178 (2019) 107456.
[16] T. Xie, C. Fang, M.S. Mohamad Ali, P. Visintin, Characterizations of autogenous and drying shrinkage of ultra-high performance concrete (UHPC): An experimental study, Cem. Concr. Compos. 91 (2018) 156–173.
[17] A.M. Soliman, M.L. Nehdi, Effects of shrinkage reducing admixture and wollastonite microfiber on early-age behavior of ultra-high performance concrete, Cem. Concr. Compos. 46 (2014) 81–89.
[18] Y. Sun, R. Yu, Z. Shui, X. Wang, D. Qian, B. Rao, J. Huang, Y. He, Understanding the porous aggregates carrier effect on reducing autogenous shrinkage of Ultra-High Performance Concrete (UHPC) based on response surface method, Constr. Build. Mater. 222 (2019) 130–141.
[19] J. Justs, M. Wyrzykowski, D. Bajare, P. Lura, Internal curing by superabsorbent polymers in ultra-high performance concrete, Cem. Concr. Res. 76 (2015) 82–90.
[20] P. Shen, L. Lu, Y. He, F. Wang, J. Lu, H. Zheng, S. Hu, Investigation on expansion effect of the expansive agents in ultra-high performance concrete, Cem. Concr. Compos. 105 (2020) 103425.
[21] P. Shen, J.-X. Lu, H. Zheng, L. Lu, F. Wang, Y. He, S. Hu, Expansive ultra-high performance concrete for concrete-filled steel tube applications, Cem. Concr. Compos. 114 (2020) 103813, https://doi.org/10.1016/j.cemconcomp.2020.103813.
[22] C. Fang, M. Ali, T. Xie, P. Visintin, A.H. Sheikh, The influence of steel fibre properties on the shrinkage of ultra-high performance fibre reinforced concrete, Constr. Build. Mater. 242 (2020) 117993.
[23] K.S. Chia, M.-H. Zhang, Water permeability and chloride penetrability of high-strength lightweight aggregate concrete, Cem. Concr. Res. 32 (4) (2002) 639–645.
[24] M.S. Nadesan, P. Dinakar, Influence of type of binder on high-performance sintered fly ash lightweight aggregate concrete, Constr. Build. Mater. 176 (2018) 665–675.
[25] B. Chen, J. Liu, Experimental application of mineral admixtures in lightweight concrete with high strength and workability, Constr. Build. Mater. 22 (2008) 1108–1113.
[26] X.F. Gao, Y.T. Lo, C.M. Tam, Investigation of micro-cracks and microstructure of high performance lightweight aggregate concrete, Build. Environ. 37 (5) (2002) 485–489.
[27] H.S. Wilson, V.M. Malhotra, Development of high strength lightweight concrete for structural applications, Int. J. Cem. Compos. Lightwght Concr. 10 (1988) 79–90.
[28] T. Wu, X. Yang, H. Wei, X. Liu, Mechanical properties and microstructure of lightweight aggregate concrete with and without fibers, Constr. Build. Mater. 199 (2019) 526–539.
[29] N.U. Kockal, T. Ozturan, Optimization of properties of fly ash aggregates for high-strength lightweight concrete production, Mater. Des. 32 (2011) 3586–3593.
[30] M. Lopez, L.F. Kahn, K.E. Kurtis, Characterization of elastic and time-dependent deformations in high performance lightweight concrete by image analysis, Cem. Concr. Res. 39 (2009) 610–619.
[31] J.A. Rossignolo, M.V.C. Agnesini, J.A. Morais, Properties of high-performance LWAC for precast structures with brazilian lightweight aggregates, Cem. Concr. Compos. 25 (2003) 77–82.
[32] R. Ahmmad, M.Z. Jumaat, U.J. Alengaram, S. Bahri, M.A. Rehman, H.b. Hashim, Performance evaluation of palm oil clinker as coarse aggregate in high strength lightweight concrete, J. Clean. Prod. 112 (2016) 566–574.
[33] P. Shafigh, M.Z. Jumaat, H.B. Mahmud, U.J. Alengaram, A new method of producing high strength oil palm shell lightweight concrete, Mater. Des. 32 (2011) 4839–4843.
[34] Y.W. Choi, Y.J. Kim, H.C. Shin, H.Y. Moon, An experimental research on the fluidity and mechanical properties of high-strength lightweight self-compacting concrete, Cem. Concr. Res. 36 (2006) 1595–1602.
[35] J. Li, J. Niu, C. Wan, X. Liu, Z. Jin, Comparison of flexural property between high performance polypropylene fiber reinforced lightweight aggregate concrete and steel fiber reinforced lightweight aggregate concrete, Constr. Build. Mater. 157 (2017) 729–736.
[36] A. Trabelsi, Z. Kammoun, Mechanical properties and impact resistance of a high-strength lightweight concrete incorporating prickly pear fibres, Constr. Build. Mater. 262 (2020) 119972, https://doi.org/10.1016/j.conbuildmat.2020.119972.
[37] J.-X. Lu, P. Shen, H. Zheng, H.A. Ali, C.S. Poon, Development and characteristics of ultra high-performance lightweight cementitious composites (UHP-LCCs), Cem. Concr. Res. 145 (2021) 106462.
[38] N. Su, K.-C. Hsu, H.-W. Chai, A simple mix design method for self-compacting concrete, Cem. Concr. Res. 31 (2001) 1799–1807.
[39] G. Hüsken, H.J.H. Brouwers, A new mix design concept for earth-moist concrete: a theoretical and experimental study, Cem. Concr. Res. 38 (10) (2008) 1246–1259.
[40] A. Habibi, J. Ghomashi, Development of an optimum mix design method for self-compacting concrete based on experimental results, Constr. Build. Mater. 168 (2018) 113–123.
[41] K. Wille, A.E. Naaman, G.J. Parra-Montesinos, Ultra-high performance concrete with compressive strength exceeding 150 MPa (22 ksi): a simpler way, ACI Mater. J. 108 (2011).
[42] R. Yu, P. Spiesz, H.J.H. Brouwers, Mix design and properties assessment of Ultra-High Performance Fibre Reinforced Concrete (UHPFRC), Cem. Concr. Res. 56 (2014) 29–39.
[43] J. Li, Y. Chen, C. Wan, A mix-design method for lightweight aggregate self-compacting concrete based on packing and mortar film thickness theories, Constr. Build. Mater. 157 (2017) 621–634.
[44] J.A. Bogas, A. Gomes, A simple mix design method for structural lightweight aggregate concrete, Mater. Struct. 46 (2013) 1919–1932.
[45] S. Jafari, S.S. Mahini, Lightweight concrete design using gene expression programing, Constr. Build. Mater. 139 (2017) 93–100.
[46] D.C. Montgomery, Design and Analysis of Experiments, John Wiley & Sons, 2017.
[47] A. Hammoudi, K. Moussaceb, C. Belebchouche, F. Dahmoune, Comparison of artificial neural network (ANN) and response surface methodology (RSM) prediction in compressive strength of recycled concrete aggregates, Constr. Build. Mater. 209 (2019) 425–436.
[48] W.E. Elemam, A.H. Abdelraheem, M.G. Mahdy, A.M. Tahwia, Optimizing fresh properties and compressive strength of self-consolidating concrete, Constr. Build. Mater. 249 (2020) 118781.
[49] M. Balcikanli Bankir, U.K. Sevim, Performance optimization of hybrid fiber concrete according to mechanical properties, Constr. Build. Mater. 261 (2020) 119952.
[50] W.N.F. Wan Hassan, M.A. Ismail, H.-S. Lee, M.S. Meddah, J.K. Singh, M.W. Hussin, M. Ismail, Mixture optimization of high-strength blended concrete using central composite design, Constr. Build. Mater. 243 (2020) 118251.
[51] S. Nunes, A.M. Matos, T. Duarte, H. Figueiras, J. Sousa-Coutinho, Mixture design of self-compacting glass mortar, Cem. Concr. Compos. 43 (2013) 1–11.
[52] M.A. Mosaberpanah, O. Eren, A.R. Tarassoly, The effect of nano-silica and waste glass powder on mechanical, rheological, and shrinkage properties of UHPC using response surface methodology, J. Mater. Res. Technol. 8 (1) (2019) 804–811.
[53] K. Ragalwar, W.F. Heard, B.A. Williams, R. Ranade, Significance of the particle size distribution modulus for strain-hardening-ultra-high performance concrete (SH-UHPC) matrix design, Constr. Build. Mater. 234 (2020) 117423, https://doi.org/10.1016/j.conbuildmat.2019.117423.
[54] I. Ferdosian, A. Camões, Eco-efficient ultra-high performance concrete development by means of response surface methodology, Cem. Concr. Compos. 84 (2017) 146–156.
[55] J.-X. Lu, P. Shen, H.A. Ali, C.S. Poon, Development of high performance lightweight concrete using ultra high performance cementitious composite and different lightweight aggregates, Cem. Concr. Compos. 124 (2021) 104277, https://doi.org/10.1016/j.cemconcomp.2021.104277.
[56] H.A. Ali, D. Xuan, C.S. Poon, Assessment of long-term reactivity of initially lowly-reactive solid wastes as supplementary cementitious materials (SCMs), Constr. Build. Mater. 232 (2020) 117192.
[57] C.M. Martín, N.B. Scarponi, Y.A. Villagrán, D.G. Manzanal, T.M. Piqué, Pozzolanic activity quantification of hollow glass microspheres, Cem. Concr. Compos. 118 (2021) 103981.

[58] A. Korpa, T. Kowald, R. Trettin, Phase development in normal and ultra high performance cementitious systems by quantitative X-ray analysis and thermoanalytical methods, Cem. Concr. Res. 39 (2009) 69–76.
[59] Y. Liu, Y. Wei, Effect of calcined bauxite powder or aggregate on the shrinkage properties of UHPC, Cem. Concr. Compos. 118 (2021) 103967.
[60] H. Du, K.H. Tan, Properties of high volume glass powder concrete, Cem. Concr. Compos. 75 (2017) 22–29.
[61] I. Mehdipour, A. Kumar, K.H. Khayat, Rheology, hydration, and strength evolution of interground limestone cement containing PCE dispersant and high volume supplementary cementitious materials, Mater. Des. 127 (2017) 54–66.
[62] R. Henkensiefken, J. Castro, D. Bentz, T. Nantung, J. Weiss, Water absorption in internally cured mortar made with water-filled lightweight aggregate, Cem. Concr. Res. 39 (2009) 883–892.
[63] M.A.A. Aldahdooh, N. Muhamad Bunnori, M.A. Megat Johari, Evaluation of ultra-high-performance-fiber reinforced concrete binder content using the response surface method, Mater. Des. (1980–2015) 52 (2013) 957-965.
[64] BS EN 12390-7, Testing hardened concrete Part 7: Density of hardened concrete, British Standard Institution, 2019.
[65] BS EN 1015-11, Methods of test for mortar for masonry Part 11-Determination of flexural and compressive strength of hardened mortar, British Standard Institution, (2019).
[66] BS EN 22007-2, Plastics – Determination of thermal conductivity and thermal diffusivity Part 2 Transient plane heat source (hot disc) method, British Standard Institution, 2015.
[67] ASTM E1050-19, Standard test method for impedance and absorption of acoustical materials using a tube, two microphones and a digital frequency analysis system, American Society of Testing Materials, 2019.
[68] ASTM E2611-19, Standard test method for normal incidence determination of porous material acoustical properties based on the transfer matrix method, American Society of Testing Materials, 2019.
[69] ASTM C1202-19, Standard test method for electrical indication of concrete's ability to resist chloride ion penetration, American Society of Testing Materials, 2019.
[70] ASTM C1585-13, Standard Test Method for Measurement of Rate of Absorption of Water by Hydraulic-Cement Concretes, American Society of Testing Materials, 2013.
[71] ASTM C1698-19, Standard Test Method for Autogenous Strain of Cement Paste and Mortar, American Society of Testing Materials, 2019.
[72] ASTM C596-18, Standard Test Method for Drying Shrinkage of Mortar Containing Hydraulic Cement American Society of Testing Materials, 2018.
[73] K. Scrivener, R. Snellings, B. Lothenbach, A Practical Guide to Microstructural Analysis of Cementitious Materials, CRC Press, New York, USA, 2016.
[74] ASTM C1856C/1856M, Standard Practice for Fabricating and Testing Specimens of Ultra-High Performance Concrete, American Society of Testing Materials, 2017.
[75] JGJT 12-2019, Technical standard for application of lightweight aggregate concrete, MOHURD (Ministry of Housing and Urban-Rural Development of the PRC), China Architecture & Building Press, Beijing, China, 2019 (in Chinese).
[76] Z. Kammoun, A. Trabelsi, A high-strength lightweight concrete made using straw, Mag. Concr. Res. 72 (2020) 460–470.
[77] S. Chandra, L. Berntsson, Lightweight Aggregate Concrete, Science, Technology and Applications, William Andrew Pulishing, New York, USA, 2003.
[78] K.-I. Horai, Thermal conductivity of rock-forming minerals, J. Geophys. Res. 76 (1971) 1278–1308.
[79] A. Dixit, S.D. Pang, S.-H. Kang, J. Moon, Lightweight structural cement composites with expanded polystyrene (EPS) for enhanced thermal insulation, Cem. Concr. Compos. 102 (2019) 185–197.
[80] S. Ng, B.P. Jelle, L.I.C. Sandberg, T. Gao, Ó.H. Wallevik, Experimental investigations of aerogel-incorporated ultra-high performance concrete, Constr. Build. Mater. 77 (2015) 307–316.
[81] M.L. Ramires, C.A. Nieto de Castro, Y. Nagasaka, A. Nagashima, M.J. Assael, W. A. Wakeham, Standard reference data for the thermal conductivity of water, J. Phys. Chem. Ref. Data 24 (1995) 1377–1381.
[82] C. Arenas, C. Leiva, L.F. Vilches, H. Cifuentes, Use of co-combustion bottom ash to design an acoustic absorbing material for highway noise barriers, Waste Manage. 33 (2013) 2316–2321.
[83] V. Tiwari, A. Shukla, A. Bose, Acoustic properties of cenosphere reinforced cement and asphalt concrete, Appl. Acoust. 65 (2004) 263–275.
[84] B. Sabir, S. Wild, M. O'farrell, A water sorptivity test for martar and concrete, Mater. Struct. 31 (1998) 568–574.
[85] N. Neithalath, Analysis of moisture transport in mortars and concrete using sorption-diffusion approach, ACI Mater. J. 103 (2006) 209.
[86] E.I. Nadelman, K.E. Kurtis, Durability of Portland-limestone cement-based materials to physical salt attack, Cem. Concr. Res. 125 (2019) 105859.
[87] N.S. Martys, C.F. Ferraris, Capillary transport in mortars and concrete, Cem. Concr. Res. 27 (1997) 747–760.
[88] M.H. Zhang, C.T. Tam, M.P. Leow, Effect of water-to-cementitious materials ratio and silica fume on the autogenous shrinkage of concrete, Cem. Concr. Res. 33 (2003) 1687–1694.
[89] P. Shen, L. Lu, Y. He, M. Rao, Z. Fu, F. Wang, S. Hu, Experimental investigation on the autogenous shrinkage of steam cured ultra-high performance concrete, Constr. Build. Mater. 162 (2018) 512–522.
[90] A.M. Neville, Properties of Concrete, Longman, London, 1995.
[91] E. Tazawa, S. Miyazawa, Influence of constituents and composition on autogenous shrinkage of cementitious materials, Mag. Concr. Res. 49 (1997) 15–22.
[92] P. Shen, L. Lu, F. Wang, Y. He, S. Hu, J. Lu, H. Zheng, Water desorption characteristics of saturated lightweight fine aggregate in ultra-high performance concrete, Cem. Concr. Compos. 106 (2020) 103456.
[93] P. Lura, M. Wyrzykowski, C. Tang, E. Lehmann, Internal curing with lightweight aggregate produced from biomass-derived waste, Cem. Concr. Res. 59 (2014) 24–33.
[94] M. Valipour, K.H. Khayat, Coupled effect of shrinkage-mitigating admixtures and saturated lightweight sand on shrinkage of UHPC for overlay applications, Constr. Build. Mater. 184 (2018) 320–329.
[95] J. Liu, C. Shi, N. Farzadnia, X. Ma, Effects of pretreated fine lightweight aggregate on shrinkage and pore structure of ultra-high strength concrete, Constr. Build. Mater. 204 (2019) 276–287.
[96] V. Baroghel-Bouny, P. Mounanga, A. Khelidj, A. Loukili, N. Rafaï, Autogenous deformations of cement pastes, Cem. Concr. Res. 36 (1) (2006) 123–136.
[97] K. Liu, R. Yu, Z. Shui, X. Li, C. Guo, B. Yu, S. Wu, Optimization of autogenous shrinkage and microstructure for Ultra-High Performance Concrete (UHPC) based on appropriate application of porous pumice, Constr. Build. Mater. 214 (2019) 369–381.
[98] Y. Ke, S. Ortola, A.L. Beaucour, H. Dumontet, Identification of microstructural characteristics in lightweight aggregate concretes by micromechanical modelling including the interfacial transition zone (ITZ), Cem. Concr. Res. 40 (2010) 1590–1600.
[99] S. Igarashi, A. Bentur, S. Mindess, Microhardness testing of cementitious materials, Adv. Cem. Based Mater. 4 (2) (1996) 48–57.
[100] A.J. Tenza-Abril, D. Benavente, C. Pla, F. Baeza-Brotons, J. Valdes-Abellan, A.M. Solak, Statistical and experimental study for determining the influence of the segregation phenomenon on physical and mechanical properties of lightweight concrete, Constr. Build. Mater. 238 (2020) 117642, https://doi.org/10.1016/j.conbuildmat.2019.117642.
[101] A.L. Brooks, H. Zhou, D. Hanna, Comparative study of the mechanical and thermal properties of lightweight cementitious composites, Constr. Build. Mater. 159 (2018) 316–328.
[102] N. Kabay, A.B. Kizilkanat, B. Akturk, Y. Kahraman, Lightweight cement-based composites incorporating hollow glass microspheres: Fresh and hardened state properties, Teknik. Dergi. 33 (2020) 1–25.
[103] W. Zhang, X. Yao, T. Yang, C. Liu, Z. Zhang, Increasing mechanical strength and acid resistance of geopolymers by incorporating different siliceous materials, Constr. Build. Mater. 175 (2018) 411–421.
[104] F. Aslani, L. Wang, Development of strain-hardening lightweight engineered cementitious composites using hollow glass microspheres, Struct. Concr. 21 (2019) 673–688.
[105] K.J. Krakowiak, R.G. Nannapaneni, A. Moshiri, T. Phatak, D. Stefaniuk, L. Sadowski, M.J. Abdolhosseini Qomi, Engineering of high specific strength and low thermal conductivity cementitious composites with hollow glass microspheres for high-temperature high-pressure applications, Cem. Concr. Compos. 108 (2020) 103514.
[106] J.-X. Lu, Z.-H. Duan, C.S. Poon, Combined use of waste glass powder and cullet in architectural mortar, Cem. Concr. Compos. 82 (2017) 34–44.
[107] M. Thomas, The effect of supplementary cementing materials on alkali-silica reaction: a review, Cem. Concr. Res. 41 (12) (2011) 1224–1231.
[108] H.K. Bas, W. Jin, N. Gupta, Chemical stability of hollow glass microspheres in cementitious syntactic foams, Cem. Concr. Compos. 118 (2021) 103928.
[109] W. Meng, K. Khayat, Effects of saturated lightweight sand content on key characteristics of ultra-high-performance concrete, Cem. Concr. Res. 101 (2017) 46–54.
[110] S. Zhutovsky, K. Kovler, A. Bentur, Influence of cement paste matrix properties on the autogenous curing of high-performance concrete, Cem. Concr. Compos. 26 (2004) 499–507.
[111] M. Wyrzykowski, S. Ghourchian, S. Sinthupinyo, N. Chitvoranund, T. Chintana, P. Lura, Internal curing of high performance mortars with bottom ash, Cem. Concr. Compos. 71 (2016) 1–9.